

The Carriers of the Unidentified Infrared Emission Features: Clues from Polycyclic Aromatic Hydrocarbons with Aliphatic Sidegroups[☆]

X.J. Yang^{a,b}, R. Glaser^c, Aigen Li^b, J.X. Zhong^{a,b}

^a*Department of Physics, Xiangtan University, 411105 Xiangtan, Hunan Province, China*

^b*Department of Physics and Astronomy, University of Missouri, Columbia, MO 65211, USA*

^c*Department of Chemistry, University of Missouri, Columbia, MO 65211, USA*

Abstract

The unidentified infrared emission (UIE) features at 3.3, 6.2, 7.7, 8.6, 11.3 and 12.7 μm are ubiquitously seen in a wide variety of astrophysical regions in the Milky Way and nearby galaxies as well as distant galaxies at redshifts $z \gtrsim 4$. The UIE features are characteristic of the stretching and bending vibrations of aromatic hydrocarbon materials. The 3.3 μm feature which results from the C–H stretching vibration in aromatic species is often accompanied by a weaker feature at 3.4 μm . The 3.4 μm feature is often thought to result from the C–H stretch of aliphatic groups attached to the aromatic systems. The ratio of the observed intensity of the 3.3 μm aromatic C–H feature ($I_{3.3}$) to that of the 3.4 μm aliphatic C–H feature ($I_{3.4}$) allows one to estimate the aliphatic fraction (e.g., $N_{\text{C,aliph}}/N_{\text{C,arom}}$, the number of C atoms in aliphatic units to that in aromatic rings) of the carriers of the UIE features, provided that the intrinsic oscillator strengths (per chemical bond) of the 3.3 μm aromatic C–H stretch ($A_{3.3}$) and the 3.4 μm aliphatic C–H stretch ($A_{3.4}$) are known. In this review we summarize the computational results on $A_{3.3}$ and $A_{3.4}$ and their implications for the aromaticity and aliphaticity of the UIE carriers. We use density functional theory and second-order perturbation theory to derive $A_{3.3}$

Email addresses: xjyang@xtu.edu.cn (X.J. Yang), glaserr@missouri.edu (R. Glaser), lia@missouri.edu (Aigen Li), jxzhong@xtu.edu.cn (J.X. Zhong)

and $A_{3.4}$ from the infrared vibrational spectra of seven polycyclic aromatic hydrocarbon (PAH) molecules with various aliphatic substituents (e.g., methyl-, dimethyl-, ethyl-, propyl-, butyl-PAHs, and PAHs with unsaturated alkyl chains). The mean band strengths of the aromatic ($A_{3.3}$) and aliphatic ($A_{3.4}$) C–H stretches are derived and then employed to estimate the aliphatic fraction of the carriers of the UIE features by comparing the ratio of the intrinsic band strength of the two stretches ($A_{3.4}/A_{3.3}$) with the ratio of the observed intensities ($I_{3.4}/I_{3.3}$). We conclude that the UIE emitters are predominantly aromatic, as revealed by the observationally-derived mean ratio of $\langle I_{3.4}/I_{3.3} \rangle \approx 0.12$ and the computationally-derived mean ratio of $\langle A_{3.4}/A_{3.3} \rangle \approx 1.76$ which suggest an upper limit of $N_{\text{C,aliph}}/N_{\text{C,arom}} \approx 0.02$ for the aliphatic fraction of the UIE carriers.

Keywords: dust, extinction — ISM: lines and bands — ISM: molecules

1. Introduction

A series of strong and relatively broad infrared (IR) emission features at 3.3, 6.2, 7.7, 8.6, 11.3, and 12.7 μm are ubiquitously seen in almost all astronomical objects with associated gas and dust, including protoplanetary nebulae (PPNe), planetary nebulae (PNe), young stellar objects, HII regions, reflection nebulae, the Galactic IR cirrus, and starburst galaxies (see Tielens 2008). These features are a common characteristic of the interstellar medium (ISM) of the Milky Way and nearby galaxies as well as distant galaxies out to redshifts of $z \gtrsim 4$ (e.g., see Riechers et al. 2014). Since their first detection four decades ago in two planetary nebulae (NGC 7027 and BD+30°3639, Gillett et al. 1973), the carriers of these IR emission features have remained unidentified. Because of this, they are collectively known as the “unidentified infrared emission” (UIE or UIR) bands. Nevertheless, it is now generally accepted that these features are characteristic of the stretching and bending vibrations of some sorts of aromatic hydrocarbon materials and therefore, the UIE features are sometimes also referred to as the “aromatic infrared bands” (AIB).

The identification of the exact carriers of the UIE bands is crucial for modern astrophysics: (1) the UIE bands account for $> 10\text{--}20\%$ of the total IR power of the Milky Way and star-forming galaxies (Tielens 2008; Smith et al. 2007), and therefore by implication, their carriers must be an important absorber of starlight in the ultraviolet (UV) wavelength region (e.g., see Joblin et al. 1992, Cecchi-Pestellini et al. 2008, Mulas et al. 2013); (2) their carriers dominate the heating of the gas in the diffuse ISM by providing photoelectrons (Lepp & Dalgarno 1988, Verstraete et al. 1990, Bakes & Tielens 1994, Weingartner & Draine 2001); (3) as an important sink for electrons, their carriers dominate the ionization balance in molecular clouds and hence they influence the ion-molecule chemistry and the ambipolar diffusion process that sets the stage for star formation (see Verstraete 2011); and (4) because of their ubiquitous presence in the ISM of the local and distant universe, the UIE bands are often taken as a reliable indicator of the star-formation rates across cosmic time up to high redshifts (see Calzetti 2011, but also see Peeters et al. 2004).

1.1. The UIE Carriers: Aromatic or Aliphatic?

A large number of candidate materials have been proposed as carriers of the UIE bands. All of these materials contain aromatic structures of fused benzene rings. The major debate lies in the exact structure of the UIE carriers: are they free-flying, predominantly *aromatic* gas-phase molecules, or amorphous solids with a *mixed aromatic/aliphatic* composition? In this context, the proposed carriers can be divided into two broad categories:

- Gas-phase, free-flying polycyclic aromatic hydrocarbon (PAH) molecules (see Figure 1a). The PAH model attributes the UIE bands to the vibrational modes of PAHs (Léger & Puget 1984; Allamandola et al. 1985, 1989), with the $3.3\ \mu\text{m}$ feature assigned to C–H stretching modes, the $6.2\ \mu\text{m}$ and $7.7\ \mu\text{m}$ features to C–C stretching modes, the $8.6\ \mu\text{m}$ feature to C–H in-plane bending modes, and the $11.3\ \mu\text{m}$ feature to C–H out-of-plane bending modes. The relative strengths of these bands depend on the chemical nature of the PAH molecule (i.e., size, structure, and

charge) and their physical environments (e.g., the intensity and hardness of the starlight illuminating the PAHs, the electron density, and the gas temperature; see Bakes & Tielens 1994, Weingartner & Draine 2001). Ionized PAHs emit strongly at 6.2, 7.7, and 8.6 μm while neutral PAHs emit strongly at 3.3 and 11.3 μm . The PAH model readily explains the UIE band patterns observed in various regions in terms of a mixture of neutral and charged PAHs of different sizes (e.g., see Allamandola et al. 1999, Li & Draine 2001). PAHs have also been proposed as a possible carrier of several other unidentified interstellar spectral features, including the diffuse interstellar bands (DIBs; see Salama et al. 2011), and the 2175 Å extinction bump (Joblin et al. 1992, Li & Draine 2001, Cecchi-Pestellini et al. 2008, Steglich et al. 2010).

- Amorphous solids with a mixed aromatic/aliphatic composition (see Figure 1 for illustration). This category includes hydrogenated amorphous carbon (HAC; Jones et al. 1990), quenched carbonaceous composites (QCC; Sakata et al. 1990), and coal or kerogen (Papoular et al. 1989). As originally suggested by Duley & Williams (1981), all of these materials share the basic molecular structure of PAHs by containing arenes.¹ They also contain aliphatic C–H bonds as well as other molecular structures often with other elements besides C and H.

1.2. HAC

HAC can be considered to be a collection of molecular clusters loosely aggregated to form an extended, three-dimensional bulk solid, with discrete aromatic “islands” embedded in a three-dimensional matrix held together unsaturated (sp and sp²) and saturated (sp³) spacers (see Figure 1b). The aromatic units

¹A benzene ring is C₆H₆. If the H atoms are gone, then it is not really “benzene” anymore. It is an aromatic ring system which can be called “arene”. Arene is a hydrocarbon with alternating double and single bonds between carbon atoms forming rings.

typically contain ~ 1 – 8 benzene rings.² Bulk HAC dust was proposed as a major constituent of interstellar grains (see Duley et al. 1989). Jones et al. (1990) argued that the probable deposition conditions of the dust in the ISM will lead to the formation of interstellar HAC. The HAC material coated on amorphous silicate dust was invoked to account for the UV and visual (UV-vis) extinction, the extended red emission (ERE; see Witt 2014). and the blue luminescence (Vijh et al. 2005). The HAC hypothesis for the UIE features postulates that the energy of the absorbed photons is localized in a small region of ~ 1 nm of the bulk, submicrometer-sized dust and therefore the aromatic islands are transiently heated to temperatures in excess of those expected for the bulk material (Duley & Williams 1988). The UIE features are thought to arise from the aromatic islands at their temperature spikes.

1.3. QCC

QCC is an experimentally-synthesized condensate of low molecular-weight hydrocarbons generated from a hydrocarbon plasma. It is synthesized by quenching the plasma of low pressure methane gas excited to high temperatures with a microwave generator (Sakata et al. 1990). The experimental conditions for making QCC are similar to what one would expect in the atmospheres of cool evolved stars where the rapid condensation of hydrocarbon dust occurs.

QCC is composed of aromatic and aliphatic molecules as well as radicals assembled in a random manner to form an amorphous solid (see Figure 1c). QCC contains four kinds of organic components such as arenes, alkynes and polyynes (CC triple bonds), olefins (CC double bonds), and saturated hydrocarbon spacers and substituents (e.g., alkyl groups). The aromatic component typically contains ~ 1 – 4 rings and mostly only one or two rings like benzene and naphthalene. These rings are connected by aliphatic chains (bridging) and can

²Compared to HAC, amorphous carbon (AC) has a smaller H content and a larger aromatic cluster size of typically ~ 20 – 40 rings and even up to several hundred rings (see Robertson 1986).

be randomly cross-linked together in a three-dimensional structure (see Sakata et al. 1990).

The QCC model interprets the 7.7 and 8.6 μm UIE bands as arising from the ketone (C=O) bond of a “cross-conjugated ketone” (CCK) molecular structure within oxidized QCC. The 6.2 μm UIE band is attributed to the C=O stretching as well as the skeletal in-plane vibration of C=C (Sakata et al. 1990). The “solo” H atoms on carbon are thought to be responsible for the 3.3 and 11.3 μm UIE features. While the oxidation of QCC may occur in the ISM, it is less likely to occur in carbon stars because of the lack of O atoms which are presumably all locked up in CO in the atmospheres of carbon stars.

1.4. Soot

Tielens (1990) argued that the condensation of carbon dust from acetylene (C_2H_2) molecules in the outflow from carbon-rich red giants is probably very similar to that occurring during the gas phase pyrolysis of hydrocarbon molecules which leads to formation of soot. Soot is a general side product of the combustion and pyrolysis of hydrocarbons such as methane, acetylene, or benzene. Soot consists of large planar PAH molecules stacked together to form platelets which are the building blocks of soot particles (see Figure 1d). These platelets as well as the layers within them are generally cross-linked by tetrahedrally bonded carbon atoms and chains (not shown in Figure 1d). The formation of soot starts from the conversion of acetylene to small PAH molecules which rapidly grow to large aromatic species. The aromatic platelets are randomly stacked to form three-dimensional structures of sizes of $\sim 1\text{--}10$ nm which further grow into soot particles by clustering and agglomeration (see Tielens 1990). Other components of soot particles include carbon nanotubes and fullerenes (see Figure 1d). C_{60} has recently been detected in a wide range of astrophysical regions (see Cami et al. 2010, Sellgren et al. 2010).

Balm & Kroto (1990) assigned the 11.3 μm UIE feature to soot-like microparticles with internal H atoms. Allamandola et al. (1985) compared the 5–10 μm Raman spectrum of auto soot with the Orion UIE bands. They found that soot

has IR spectral features in close correspondence to that seen in space.

1.5. Coal and Kerogen

Papoular et al. (1989) were the first ones to draw attention to coal as a possible model for understanding the UIE bands. They showed that the absorption spectra of vitrinite, the major organic component of demineralized coal, resemble the observed UIE bands. Coal is mainly composed of C, H, and O and differs from HAC partly by its higher oxygen content (~ 2 to 20% by mass). A large fraction of the carbon in coal is in the form of condensed aromatic units arranged in graphite-like “bricks”. These “basic structural units” (of ~ 1.5 nm in size) are randomly oriented and made of stacks of a few layers of planar arene systems packed together to form an irregular carbon skeleton (see Figure 1e). Most of the H atoms are bonded to this carbon skeleton, while O atoms bridge the gaps between the “bricks”. H and O form, together with C, simple functional groups attached to the inter-connected “bricks” that are responsible for the vibrational bands that mimic the UIE bands.

The IR spectra of coal differ considerably according to the coal history which is quantified by its “rank”, “order” or carbon content (or, equivalently, its age, or the mining depth of the seam in which it originated). As coal ages, the concentration of H and O in it decreases and the C content increases. With increasing C content, H/C decreases, O/C decreases, aromaticity increases, the degree of substitution in aromatic rings decreases and the rank or order of coal improves. For high ranking coals (with a carbon-content of $>90\%$), the intensity of the aromatic C–H stretching band relative to that of the aliphatic band increases very steeply as a result of a decrease of the number of aliphatic H atoms and an increase of the aromatic H atoms. According to Papoular et al. (1989), the average UIE carrier is best mimicked by anthracite, the highest ranking coal (i.e., most graphite-like).

Papoular (2001) analyzed the absorption spectra of terrestrial kerogen materials and argued that kerogen could explain the observed UIE features. Kerogen is a family of highly disordered macromolecular organic materials made of C,

H and O, and traces of N and S (see Figure 1e). It is a solid sedimentary, insoluble organic material found in the upper crust of the Earth in dispersed form. The main difference between kerogen and coal is that the latter is found in the form of bulk rocks and the former in dispersed form (sand-like). The term kerogen is also often used to designate the insoluble, three-dimensional, organic macromolecular skeleton which is the main constituent of coal. Upon aging, kerogen changes its composition with oxygen expelled in the form of CO, CO₂ and H₂O and hydrogen expelled in the form of methane (CH₄). This will break the aliphatic chains and allow aromatic rings to form and coalesce in clusters in kerogen and therefore increase its aromaticity. Papoular (2001) argued that the great diversity of the astronomical UIE spectra could be explained by kerogen of different evolutionary stages characterized by different ratios of O to C concentrations, and of H to C concentrations.

Cataldo et al. (2013) compared the UIE features observed in some PPNe with the experimentally-measured absorption spectra of heavy petroleum fractions and asphaltenes. A series of heavy petroleum fractions (e.g., “distillate aromatic extract”, “residual aromatic extract”, heavy aromatic fraction (BQ-1) and asphaltenes derived from BQ-1) were considered. They found that the band pattern of the UIE features (particularly that of the aromatic-aliphatic C–H stretching bands) of certain PPNe is closely matched by the BQ-1 heavy aromatic oil fraction and by its asphaltene fraction. Like coal or kerogen, the heavy petroleum fractions contain a mix of aromatic and aliphatic structures. They are composed of aromatic cores containing three to four condensed aromatic rings surrounded by cycloaliphatic (naphthenic) and aliphatic alkyl chains. In comparison with coal, the heavy petroleum fractions are viscous liquids at room temperature and become glassy solids below ~ 235 K.

1.6. Excitation Mechanism: Equilibrium Temperatures or Stochastic Heating?

The HAC, QCC, and coal/kerogen hypotheses all assume that the UIE bands arise following photon absorption in small thermally-isolated aromatic units within or attached to these bulk materials. However, it does not appear

possible to confine the absorbed stellar photon energy within these aromatic “islands” for the time $\gtrsim 10^{-3}$ s required for the thermal emission process (see Li & Draine 2002). Bulk materials like HAC, QCC and coal have a huge number of vibrational degrees of freedom and therefore their heat capacities are so large that they will attain an equilibrium temperature of $T \sim 20$ K in the diffuse ISM (see Li 2004). With $T \sim 20$ K, they will not emit efficiently in the UIE bands at $\lambda \sim 3\text{--}12 \mu\text{m}$ (Draine & Li 2007).

It has been observationally demonstrated that the UIE profiles remain constant even the exciting starlight intensities vary by five orders of magnitude (e.g., see Boulanger et al. 1999). The equilibrium temperature T depends on the starlight intensity U [e.g., $T \propto U^{1/(4+\alpha)}$ if the far-IR emissivity of the dust is proportional to $\lambda^{-\alpha}$]. Therefore, if the UIE bands arise from bulk materials like HAC, QCC, or coal, one would expect the UIE profiles to vary with the starlight intensity. Furthermore, Sellgren et al. (1983) also showed that in some reflection nebulae the UIE profiles and the color temperatures of the smooth continuum emission underneath the $3.3 \mu\text{m}$ UIE feature show very little variation from source to source and within a given source with distance r from the central star. Sellgren (1984) argued that the UIE features and the associated continuum emission could not be explained by thermal emission from bulk dust in radiative equilibrium with the central star. Otherwise one would expect them to vary with r as the equilibrium temperature T of bulk dust is expected to decline with r : $T \propto r^{-2/(4+\alpha)}$.

Recognizing the challenge of bulk materials like HAC, QCC and coal in being heated to emit the UIE bands, Kwok & Zhang (2011, 2013) recently proposed the so-called MAON model: they argued that the UIE bands arise from coal- or kerogen-like organic nanoparticles, consisting of chain-like aliphatic hydrocarbon material linking small units of aromatic rings, where MAON stands for “*mixed aromatic/aliphatic organic nanoparticle*” (see Figure 1f). The major improvement of the MAON model over the earlier HAC, QCC and coal hypotheses is that the MAON model hypothesizes that the coal-like UIE carriers are *nanometer* in size so that their heat capacities are smaller than or compara-

ble to the energy of the starlight photons that excite them. Upon absorption of a single stellar photon, they will be stochastically heated to high temperatures to emit the UIE bands (see Draine & Li 2001). The stochastic heating nature of PAHs guarantees that the UIE spectra (scaled by the starlight intensity) to remain the same for different starlight intensities.³ This is true for both hard radiation fields and soft radiation fields (see Draine & Li 2001, Li & Draine 2002). As demonstrated in Figure 1f of Draine & Li (2007), the UIE spectra predicted from the PAH model are essentially the same even if the illuminating starlight intensities differ by a factor of 10^5 .

To summarize, it is fair to conclude that, based on the brief descriptions of the proposed carriers presented above, the current views about the UIE carriers generally agree that (1) the UIE features arise from the *aromatic* C–C and C–H vibrational modes, and (2) the carriers must be *nanometer* in size or smaller (e.g., large molecules). The dispute is mainly on the structure of the UIE carriers: are they predominantly *aromatic* (like PAHs), or *largely aliphatic* but mixed with small aromatic units (like MAONs)?

1.7. Are the UIE Carriers Aromatic or Aliphatic? Constraints from the C–H Stretching Features

Are the UIE carriers aromatic or aliphatic? A straightforward way to address this question is to examine the *aliphatic fraction* of the UIE carriers (i.e., the fraction of carbon atoms in aliphatic chains). Aliphatic hydrocarbons have a vibrational band at $3.4\ \mu\text{m}$ due to the C–H stretching mode (Pendleton & Allamandola 2002). In many interstellar and circumstellar environments the $3.3\ \mu\text{m}$ emission feature is indeed often accompanied by a weaker feature at $3.4\ \mu\text{m}$ (see Figure 2 for illustration). As demonstrated by Li & Draine (2012) and Yang et al. (2013), one can place an upper limit on the aliphatic fraction of

³Single-photon heating implies that the shape of the high- T end of the temperature (T) probability distribution function for a nanoparticle is the same for different levels of starlight intensity, and what really matters is the mean photon energy (which determines to what peak temperature a nanoparticle will reach upon absorption of such a photon).

the emitters of the UIE features by assigning the 3.4 μm emission *exclusively* to aliphatic C–H (also see Rouillé et al. 2012, Steglich et al. 2013).⁴ This requires the knowledge of the intrinsic oscillator strengths of the 3.3 μm aromatic C–H stretch ($A_{3.3}$) and the 3.4 μm aliphatic C–H stretch ($A_{3.4}$), where $A_{3.3}$ and $A_{3.4}$ are on a per unit C–H bond basis.

In this review we summarize our recent work on computing the IR vibrational spectra of a range of PAH molecules with various aliphatic sidegroups (e.g., methyl-, dimethyl-, ethyl-, propyl-, butyl-PAHs, and PAHs with unsaturated alkyl chains), based on density functional theory and second-order perturbation theory. The mean band strengths of the aromatic and aliphatic C–H stretches are derived and then employed to estimate the aliphatic fraction of the carriers of the UIE features by comparing the ratio of the intrinsic band strength of the two stretches with the ratio of the observed intensities.

In §2 we describe the computational methods and the parent molecules based on which we derive the band strengths of the aromatic and aliphatic C–H stretches. The structures and stabilities of methylated PAHs are discussed in §3. We report in §4.1 the computed frequencies and intensities of the C–H stretching modes of the parent PAHs as well as that of their methylated derivatives in §4.2. Theoretical level dependencies of the computed band intensities and approaches to intensity scaling are discussed in detail in §5. In §6 we present the recommended mean band intensities for the aromatic and aliphatic C–H stretches. We estimate in §7 the aliphatic fraction of the UIE carriers from the mean ratio of the observed intensities of the 3.3 μm aromatic and 3.4 μm aliphatic C–H features. We summarize our major results in §8.

A considerable fraction of this review is concerned with the computational techniques and the resulting frequencies and intensities for the aromatic and aliphatic C–H stretching modes of a range of PAHs and their methylated deriva-

⁴This is indeed an *upper limit* as the 3.4 μm emission feature could also be due to *anharmonicity* of the aromatic C–H stretch (Barker et al. 1987) and “*superhydrogenated*” PAHs whose edges contain excess H atoms (Bernstein et al. 1996, Sandford et al. 2013).

tives. For more details we refer the interested readers to Yang et al. (2016a,b, 2017). Readers who are interested only in the mean ratio of the band strength of the $3.4\ \mu\text{m}$ aliphatic C–H stretch to that of the $3.3\ \mu\text{m}$ aromatic C–H stretch ($A_{3.4}/A_{3.3}$) and their implications for the aliphatic fraction of the UIE carriers may wish to proceed directly to §6.

2. Computational Methods and Target Molecules

We use the Gaussian09 software (Frisch et al. 2009) to calculate the IR vibrational spectra for a range of aromatic molecules with a methyl side chain (see Figure 3). We have considered benzene (C_6H_6), naphthalene (C_{10}H_8), anthracene ($\text{C}_{14}\text{H}_{10}$), phenanthrene ($\text{C}_{14}\text{H}_{10}$), pyrene ($\text{C}_{16}\text{H}_{10}$), perylene ($\text{C}_{20}\text{H}_{12}$), and coronene ($\text{C}_{24}\text{H}_{12}$), as well as all of their methyl derivatives (see Figure 3).

We employ the hybrid density functional theoretical method (B3LYP) in conjunction with a variety of basis sets: 6-31G*, 6-31+G*, 6-311+G*, 6-311G**, 6-31+G**, 6-31++G**, 6-311+G**, 6-311++G**, 6-311+G(3df,3pd), and 6-311++G(3df,3pd). Here the Slater-type atomic orbitals (AOs) are described by one or more “basis functions (BFs)” and each basis function usually is described by a sum of several Gaussian functions with various radial distributions (reflected in the exponents). For example, the “6” in 6-31G* indicates that every core AO is described by one basis function which is expressed as a sum of 6 “primitive” Gaussian functions. The “31” part describes a “split-valence” basis set, that is, every valence AO is described by two independently varied basis functions, and it is primarily this feature that allows the electron density to adopt the best radial distribution for any given bonding situation. Similarly, “-311” refers to a “triply-split valence” basis set (3 basis functions for every valence AO) and allows for even more freedom to describe the electronic wave function. While atomic orbitals have perfect s- and p-shapes, the electron density distributions within molecules are polarized (oriented) and so-called “polarization functions” are added to the basis set to allow for an improved description of this polarization around atoms. Small admixtures of p-type basis functions polarize

s-type AOs, small admixtures of d-type BFs polarize p-AOs, small admixtures of f-type BFs polarize d-AOs, etc. Information about the types and number of polarization functions is provided after the “G” in the basis set descriptor, first for non-H atoms and then for H-atoms. For example, that large basis set 6-311+G(3df,3pd) contains three sets of d-functions and one set of f-functions on every carbon atom and it contains three sets of p-functions and one set of d-functions on every hydrogen. The basis set 6-31G** denotes 6-31G(d,p). “Diffuse functions” are spatially rather extended basis functions and they are important to reproduce electric multipoles with high accuracy. The augmentation of a basis set with diffuse functions is indicated by “+” signs, where the first “+” refers to heavy atoms (C in our cases) and the second “+” refers to H-atoms. In general, the quality of the wave function improves with the number of basis functions, with the number of primitives per basis function, with the number of polarization functions, and with the extent of diffuse-function augmentation. Since computer-time needs scale exponentially with the number of basis functions N , the art consists in understanding the essential requirements.

We also employ second-order Møller-Plesset perturbation theory (hereafter abbreviated as MP2) in conjunction with the basis sets 6-311+G** and 6-311++G(3df,3pd) for some of the molecules. The MP2 computations were performed either with the full active space of all core and valence electrons considered in the correlation energy computation, denoted MP2(full), or with the frozen core approximation and the consideration of just the valence electrons in the correlation treatment, denoted MP2(fc).

In this work all molecules are optimized and calculated at B3LYP/6-31G*. Benzene, toluene and naphthalene and methylnaphthalenes are studied using several theoretical levels: B3LYP/6-311+G**, B3LYP/6-311+G(3df,3pd), MP2/6-311+G**, and MP2/6-311+G(3df,3pd). Toluene and isomers of methylpyrene are studied at B3LYP using basis sets from 6-31G* all the way up to 6-311++G(3df,3pd). Scaling will be applied to frequencies and intensities. We employ the frequency scale factors recommended for the various theoretical levels (see Borowski 2012, Andersson et al. 2005, Merrick et al. 2007) and their values are listed in Ta-

ble 1. For the intensity scaling factors, we will discuss in detail in §5 regarding the theoretical level dependency of the computed band intensities.

3. Structures and Stabilities of Methylated PAHs

The molecules studied are shown in Figure 3 together with the standard *International Union of Pure and Applied Chemistry* (IUPAC) numbering scheme.⁵ We use the first four letters of the molecules to refer to them and attach the position number of the location of the methyl group. For example, 1-methylnaphthalene is referred to as Naph1. The methyl conformations are indicated in Figure 3 and there are several possibilities.

Depending on the symmetry of the molecule, there are one or two stereoisomers in which one of the methyl-CH bonds lies in the plane of the arene. We differentiate between these stereoisomers by addition of “*a*” or “*b*” to the name of the structure isomer, and the in-plane C–H bond points into the less (more) crowded hemisphere in the *a*-conformation (*b*-conformation).⁶ In most cases, either the *a*-conformation or the *b*-conformation corresponds to the minimum while the other conformation corresponds to the transition state structure for methyl rotation.⁷ Note that the *a*-conformation can be the minimum (i.e., Naph1a) or the rotational transition state structure (i.e., Naph2a).

⁵<http://www.iupac.org>

⁶Take Naph1a and Naph1b as examples. In Naph1a, the in-plane methyl-H is four bonds away from the closest H-atom, H at C2. In Naph1b, the in-plane methyl-H is five bonds away from the closest H-atom, H at C8. This leaves more space between the in-plane methyl-H and H(C2) in Naph1a than between in-plane methyl-H and H(C8) in Naph1b, and Naph1a is less crowded than Naph1b.

⁷A structure on the potential energy surface is a “stationary structure” if the net interatomic forces on each atom is acceptably close to zero. A “minimum” is a stationary structure for which a small distortion along any internal coordinate increases the energy (all curvatures are positive). A “transition state structure” is a stationary structure for which a small distortion along one internal coordinate lowers the energy while distortions along any of the other internal coordinates increases the energy. The internal coordinate with the negative curvature is called the “transition vector”. For the rotational transition state structures, the transition vector describes a rotation of the methyl group about the H₃C–C bond and serves to scramble

The molecules Tolu, Anth9 and Pyre2 are symmetric and the *a*- and *b*-conformations are identical. In these cases there exists an additional conformation type, the *c*-conformation, in which one of the methyl-CH bonds is almost perpendicular with respect to the arene plane. For Tolu and Pery2, the *c*-conformation is the minimum while the conformations with in-plane CH-bonds are the rotational transition state structures. In contrast, for Anth9 the *c*-conformation serves as the transition state for interconversion between the conformations with in-plane CH-bonds.

The structures are generally unremarkable. In most cases the *a*-, *b*- and *c*-conformations all feature essentially planar arenes and only Phen4 and Pery1 stand out and their structures are shown in Figure 4. While there is no problem to accommodate the in-plane CH-bond in Phen4a, a Phen4b-type structure is prohibited because of the extraordinary steric interaction between the in-plane methyl CH-bond and the C(5)H-bond.⁸ It is required that the entire methyl group is bent out of the best arene plane to accomplish the methyl rotation via the transition state structure Phen4c. In the case of Pery1, the steric repulsion between the methyl group and the C(12)H-bond is so strong that both the minimum Pery1c and the transition state structure Pery1d contain twisted perylene moieties and, in both structures, the methyl group is moved out of the best plane of the arene to which it is attached. Note that one methyl-CH bond is nearly perpendicular to the attached arene Pery1c and Pery1d. The difference between Pery1c and Pery1d concerns the orientation of this near-perpendicular CH bond relative to the other naphthalene moiety (the one without the methyl group); it points either to (in Pery1c) or away (in Pery1d) from the best plane of the other naphthalene.

The structure of Phen4a is no longer C_s -symmetric: the “in-plane” CH-bond

the H atoms in the associated minimum structures (i.e., Naph1a can be realized with any one of the three methyl-Hs in the plane).

⁸C(5) stands for the carbon atom numbered 5 in the corresponding molecule as marked in Figure 3.

is slightly out of the plane ($\angle(\text{H-C-C4-C3}) = 9.5^\circ$), the methyl-C no longer lies in the arene plane ($\angle(\text{H}_3\text{C-C4-C3-C2}) = 177.3^\circ$), and the phenanthrene frame is twisted significantly ($\angle(\text{C4-C4a-C4b-C5}) = 8.2^\circ$). In Phen4c, one CH-bond is almost perpendicular to the attached benzene plane ($\angle(\text{H-C-C4-C3}) = 83.1^\circ$), the methyl-C is moved more out of the plane of the attached benzene ($\angle(\text{H}_3\text{C-C4-C3-C2}) = 167.4^\circ$), and the phenanthrene frame twisting grows significantly ($\angle(\text{C4-C4a-C4b-C5}) = 20.6^\circ$).⁹ As can be seen, in Pery1c the two naphthalene moieties are twisted significantly ($\angle(\text{C6b-C6a-C12b-C12a}) = 13.9^\circ$) and the methyl group also is slightly pushed out of the arene plane and away from the H atom at C12 ($\angle(\text{H}_3\text{C-C1-C2-C3}) = 176.4^\circ$). In the transition state structure Pery1d both of these deformations are enhanced with $\angle(\text{C6b-C6a-C12b-C12a}) = 13.9^\circ$ and $\angle(\text{H}_3\text{C-C1-C2-C3}) = 170.5^\circ$.

4. Results

All of the molecules are studied in all conformations at the B3LYP/6-31G* level and the computed total energies and the thermochemical parameters are summarized in Table 2 for the minima and in Table 3 for the transition states. For reasons that will be given below, the minima of all of the molecules are also studied at the B3LYP/6-311+G** level. Table 4 lists the computed total energies and the thermochemical parameters obtained at the B3LYP/6-311+G** level.

The vibrational frequencies and intensities for the aromatic and the methyl (aliphatic) C-H stretching modes were computed. The standard scaling is applied to the frequencies by employing the scale factors listed in Table 1. The scaling for the intensities will be discussed in §5.

The calculations always show three methyl C-H stretches for all the methyl derivatives of all the molecules, and we always describe these three bands as $\nu_{\text{Me},1}$, $\nu_{\text{Me},2}$, and $\nu_{\text{Me},3}$ as illustrated in Figure 5. For demonstration, we show

⁹C4(a) stands for the carbon atom numbered 4a in the corresponding molecule as marked in Figure 3.

in Table 5 the frequencies and intensities computed at some of the levels for toluene along with the gas-phase experimental data of Wilmshurst & Bernstein (1957) and of the *National Institute of Standards and Technology* (NIST).¹⁰

4.1. Frequencies and Intensities of Parent PAHs

4.1.1. Benzene

Selected computed spectra of benzene are shown in Figure 6 together with the experimental gas-phase spectrum taken from NIST. The computed spectrum shows just one band which corresponds to the fundamental mode ν_{12} in the Herzberg nomenclature (Herzberg 1945). The experimental gas phase spectrum shows three bands at 3045, 3073 and 3099 cm^{-1} and only the last one of these is a pure C–H vibration. The measured ν_{12} band appears at $\sim 3099 \text{ cm}^{-1}$ and it is about 22 cm^{-1} above the scaled computed frequency because of Fermi resonance (FR; Herzberg 1945). The pure C–H stretching mode ν_{12} (at $\sim 3076 \text{ cm}^{-1}$ without FR) forms a resonance doublet with the combination band ($\nu_{13} + \nu_{16}$) which shows a similar offset of $\sim 23.8 \text{ cm}^{-1}$ in the opposite direction ($\nu_{13} = 1485 \text{ cm}^{-1}$; $\nu_{16} = 1584.8 \text{ cm}^{-1}$). The quantitative NIST spectrum¹¹ gives an absorption intensity of $\sim 54.4 \text{ km mol}^{-1}$ for the aromatic C–H stretches in benzene in gas phase, and this value is in close agreement with the intensity of $\sim 55 \text{ km mol}^{-1}$ reported by Pavlyuchko et al. (2012). On the other hand, Bertie & Keefe (1994) gave a significantly higher value of $A_{\text{aro}}(\nu_{12}) \approx 73 \pm 9 \text{ km mol}^{-1}$ based on their integration over the range of $3175\text{--}2925 \text{ cm}^{-1}$. This region contains some intensity from the (weak) combination bands and all the experimental intensity data are much lower than the value $A_{\text{aro}}(\nu_{12}) \approx 104 \text{ km mol}^{-1}$ computed at the B3LYP/6-31G* level. Clearly, we will need to take a closer look at the accuracy of the computed intensities.

¹⁰<http://webbook.nist.gov>

¹¹The intensities for benzene are taken from the 3-term Blackman-Harris entries with a resolution of 0.125 cm^{-1} .

4.1.2. Important Parent PAHs

The NIST experimental spectra of the non-substituted PAHs (naphthalene, anthracene, phenanthrene, and pyrene) are shown in Figure 6 together with selected computed spectra. The experimental spectra of these PAHs always show one strong band at $\sim 3050\text{ cm}^{-1}$ for the aromatic C–H stretches and several weak bands in the region of $2800\text{--}3000\text{ cm}^{-1}$. These NIST spectra are not a part of the NIST *Quantitative Infrared Database* and therefore there is no intensity information in the NIST database. The gas-phase intensity measurements of the aromatic C–H stretches have been reported for naphthalene ($\sim 96\text{ km mol}^{-1}$; Cané et al. 1996, Pauzat et al. 1999), anthracene ($\sim 161\text{ km mol}^{-1}$; Cané et al. 1997, Pauzat et al. 1999), pyrene ($\sim 122\text{ km mol}^{-1}$; Joblin et al. 1994, Pauzat et al. 1999), and coronene ($\sim 161\text{ km mol}^{-1}$; Joblin et al. 1994). It appears that no gas phase IR intensities have been published for phenanthrene and perylene.

Visual inspection of Figure 6 shows that good to excellent agreement between the measured and computed C–H stretch vibrational frequencies can be achieved in all cases with the use of standard scale factors. The computed spectra are usually drawn with the line broadening set to be 4 cm^{-1} . Note especially that the weak features in the range of $2800\text{--}3000\text{ cm}^{-1}$ (due to overtones and combinations, Mitra & Bernstein 1959) are much weaker for the parent PAHs as compared to benzene itself (vide supra).

Again, the experimental intensities are much lower than our calculated results for the aromatic C–H stretches at B3LYP/6-31G* level. With the calculated intensity $A_{\text{aro}}(\text{cal})$ and the experimental value $A_{\text{aro}}(\text{exp})$, we find positive values for $\Delta A = A_{\text{aro}}(\text{cal}) - A_{\text{aro}}(\text{exp})$: naphthalene [$A_{\text{aro}}(\text{cal}) \sim 139\text{ km mol}^{-1}$, $\Delta A = A_{\text{aro}}(\text{cal}) - A_{\text{aro}}(\text{exp}) \approx 43\text{ km mol}^{-1}$], anthracene [$A_{\text{aro}}(\text{cal}) \sim 178\text{ km mol}^{-1}$, $\Delta A \approx 17\text{ km mol}^{-1}$], pyrene [$A_{\text{aro}}(\text{cal}) \sim 188\text{ km mol}^{-1}$, $\Delta A \approx 66\text{ km mol}^{-1}$], and coronene [$A_{\text{aro}}(\text{cal}) \sim 257\text{ km mol}^{-1}$, $\Delta A \approx 96\text{ km mol}^{-1}$].

4.2. Frequencies and Intensities of Toluene and Methylated PAHs

4.2.1. Toluene

Selected computed spectra of toluene are shown in Figure 7 together with the experimental spectra taken from NIST and from Wilmshurst & Bernstein (1957). The experimental spectra are similar, and both contain just two bands in the methyl region and also two bands in the aromatic region. The wavenumbers of those maxima are shown in Table 5.

It is clear from Figure 7 that the standard scaling works well for the aromatic C–H stretches. For the methyl (aliphatic) C–H stretches, it is remarkable that the computations (after normal scaling) greatly overestimate the frequencies of the asymmetric modes $\nu_{\text{Me},2}$, $\nu_{\text{Me},3}$, while $\nu_{\text{Me},1}$ is somewhat underestimated. This remarkable discrepancy is a consequence of the harmonic approximation and the free rotation of the methyl group. For our present purposes, it is important to recognize that the experimental value of $A_{\text{ali}}(\text{exp})$ – the intensity of all the methyl (aliphatic) C–H stretches – does contain a substantial contribution from overtones (about 19%).

In the absence of absolute intensity data for most of the molecules in our set, we will discuss the ratio of the intensities in the regions of the methyl (aliphatic) and aromatic C–H stretches and this ratio is determined as follows. We digitize the NIST experimental spectra and integrate over the selected regions. We take 3000 cm^{-1} as the wavenumber separation of the methyl (aliphatic) and aromatic C–H stretching regions. The integration over the range of $3000\text{--}3200\text{ cm}^{-1}$ is taken as the total intensity of the aromatic C–H stretches (A_{aro}). Similarly, the integration in the range of $2800\text{--}3000\text{ cm}^{-1}$ is taken as the total intensity of the aliphatic C–H stretches (A_{ali}). The relative intensity of the methyl (aliphatic) signal to that of the aromatic band is $A_{\text{ali}}/A_{\text{aro}} \approx 0.79$. A similar analysis of the spectrum of Wilmshurst & Bernstein (1957) results in the experimental methyl signal intensity of $A_{\text{ali}}/A_{\text{aro}} \approx 0.71$ relative to that of the aromatic C–H band. Note that A_{aro} (A_{ali}) is the strength of all the aromatic (aliphatic) C–H stretches while $A_{3,3}$ ($A_{3,4}$) is the strength of the aromatic (aliphatic) stretch per

C–H bond. For toluene, $A_{\text{aro}} = 5A_{3.3}$ and $A_{\text{ali}} = 3A_{3.4}$ and therefore we have $A_{3.4}/A_{3.3} = (5/3) A_{\text{ali}}/A_{\text{aro}}$.

Our integration of the NIST spectrum gives a total intensity of $\sim 97.2 \text{ km mol}^{-1}$ for all the C–H stretches (both methyl and aromatic) and is in excellent agreement with the value of $\sim 95 \text{ km mol}^{-1}$ reported by Pavlyuchko et al. (2012) and by Galabov et al. (1992). According to our ratio of the measured intensities for the methyl to aromatic regions ($A_{\text{ali}}/A_{\text{aro}} \approx 0.79$), this overall intensity corresponds to intensities of $\sim 42.9 \text{ km mol}^{-1}$ for the methyl bands and of $\sim 54.3 \text{ km mol}^{-1}$ for the aromatic bands. The intensities computed at the B3LYP/6-31G* level for toluene are $\sim 165.3 \text{ km mol}^{-1}$ for the entire region and ~ 70.4 and $\sim 94.9 \text{ km mol}^{-1}$ for the methyl and aromatic sections, respectively. Again, we see that the computed intensities are much higher than the experimental values from the gas phase measurements.

4.2.2. Important Methylated PAHs

Selected computed spectra of all the monomethyl-substituted PAHs (naphthalene, anthracene, phenanthrene, and pyrene) are shown in Figure 8 together with the corresponding gas-phase experimental spectra taken from NIST (if available). As expected, the NIST spectra of the methyl-PAHs show several strong bands in the region $3040\text{--}3070 \text{ cm}^{-1}$ due to the aromatic C–H stretching modes. In all of these spectra, the computed spectra with standard wavenumber scaling are shown with a line width of 4 cm^{-1} .

The interesting aspect of Figure 8 concerns the bands due to the methyl (aliphatic) C–H stretches in the region $2800\text{--}3000 \text{ cm}^{-1}$. As with toluene, the first band on the low-wavenumber side in the experimental spectra is due to overtones, and the remaining band(s) in the aliphatic region are due to the overlapping methyl C–H stretches. The computed spectrum of Anth9 stands out in that $\nu_{\text{Me},3}$ is extraordinarily high and appears in the aromatic region ($\nu_{\text{Me},3} \approx 3048 \text{ cm}^{-1}$). Pauzat et al. (1999) reported a similar $\nu_{\text{Me},3} \approx 3030 \text{ cm}^{-1}$ for Anth9. Hence, one must wonder whether part of the intensity of the “aromatic region” is due to the aliphatic C–H stretching mode $\nu_{\text{Me},3}$.

To address this question, we also compute the anharmonic vibrations at the B3LYP/6-31G* level for Anth9 (see Figure 8, the green line in the Anth9 panel). We again find that $\nu_{\text{Me},2}$ and $\nu_{\text{Me},3}$ are overestimated by $\sim 48 \text{ cm}^{-1}$ and $\sim 6 \text{ cm}^{-1}$ respectively, and $\nu_{\text{Me},1}$ is underestimated by $\sim 53 \text{ cm}^{-1}$ in the harmonic approximation (even after scaling). However, even with the anharmonic approximation, $\nu_{\text{Me},3}$ is still in the aromatic region, hence, we conclude that the aliphatic and aromatic regions do overlap in the experimental spectrum of Anth9.

The unusual behavior of Anth9a results from the fact that one methyl C–H bond lies in the arene plane and stretches of this C–H bond cannot occur independently of stretches of the proximate C(1)–H bond, i.e., the presence of an all-*cis* H–C_{Me}–(C_{aro})3–H moiety. Instead, the stretching of the in-plane methyl CH bond must be out of phase with any stretching of the C(1)–H bond to avoid steric repulsion. This coupling is illustrated schematically in the bottom row of Figure 5. This structural feature of Anth9a is uncommon in minima of other PAHs, but it is common in transition state structures and this type of vibrational coupling also occurs in Naph1b, Anth1b, Phen1b, Phen9b, Pyre1b, Pyre4b, Pery3b and Coro1b. The structural feature is not present in the isomers Anth1a and Anth2b, and the vibrational spectra of the minima of the anthracene isomers therefore are not expected and do not show the coupling of Anth9a.

Again, we integrate the aromatic C–H stretches to obtain A_{aro} and integrate the methyl (aliphatic) C–H stretches to obtain A_{ali} . The intensity of the methyl signals relative to that of the aromatic stretches are generally $A_{\text{ali}}/A_{\text{aro}} \sim 0.53$ at B3LYP/6-31G*. The only exception is 9-methylanthracene (Anth9) with its much smaller relative intensity of $A_{\text{ali}}/A_{\text{aro}} \sim 0.42$. Considering that the aliphatic C–H stretch ($\nu_{\text{Me},3}$) contributes to the aromatic region, this is not surprising.

5. Theoretical Level Dependency of Computed IR Intensities

5.1. B3LYP vs. MP2 IR Intensities of C–H Stretching Modes

As we have seen above, the IR intensities calculated at the B3LYP/6-31G* level are much higher compared to the experimental results. Using better basis sets in conjunction with the B3LYP method, we found that the IR intensities still differ by a factor of $\sim 30\%$ compared to the experiment results (see Table 6). Pavlyuchko et al. (2012) recently reported that the IR intensities calculated for benzene and toluene at the level MP2/6-311G(3df,3pd) would match the experimental results very well. Considering this report, we try to reproduce their data for benzene and toluene and we perform both MP2(fc) and MP2(full) computations with the 6-311G(3df,3pd) basis set. The MP2(fc) results closely match the data of Pavlyuchko et al. (2012; see Table 6). The IR intensities computed with and without the frozen core (fc) approximation actually differ noticeably for toluene and, hence, we then calculate all other vibrational spectra with the MP2(full) method in conjunction with the standard basis set 6-31G* and the extended basis sets 6-311+G** and 6-311+G(3df,3pd) for benzene, naphthalene and their mono-methyl derivatives as test cases. The most relevant results are given in Table 6.

Note that the addition of sets of diffuse functions in the large basis set 6-311+G(3df,3pd) drastically changes the IR intensities for benzene and toluene. This level is better than the MP2(full)/6-311G(3df,3pd) level and at this level the overall intensities are significantly lower than the experimental data. This finding shows that the seemingly excellent agreement between experiment and the MP2(fc)/6-311G(3df,3pd) data is fortuitous. Second, this finding actually makes perfect sense because the experimental IR intensities in the C–H stretching regions always contain significant contributions from overtones and combinations (*vide supra*). The overtones in the methyl region of toluene are responsible for $\sim 19\%$ of the intensity. Subtraction of 19% of the intensity of the methyl region results in the adjusted experimental value of $\sim 89.0 \text{ km mol}^{-1}$, and this value is in excellent agreement with the computed value of 86.5 km mol^{-1} .

While the MP2(full)/6-311+G(3df,3pd) level data reproduce the measured IR intensities reasonably well, such calculations are far too expensive especially for the larger molecules. The MP2(full) computations of the naphthalene systems with the large basis sets including the (3df,3pd) polarization functions each requires several days of computer time on eight processors. Considering that the absolute values computed at all of the MP2 levels are better than the respective values computed at the B3LYP levels, one would be inclined to explore scaling approaches of the MP2 data computed with modest basis sets. However, we will show that scaling approaches that are based on the B3LYP data can be just as successful in spite of the fact that the absolute numbers computed at the B3LYP/6-31G* level differ much more from experiment than do the MP2/6-31G* data.

Before we proceed, it is useful to clarify the meaning of scaling approaches. In the most typical approach to scaling, it is attempted to reproduce a set of experimental data with a set of data obtained at a level L_i such that $p(\text{exp}) \approx f \cdot p(L_i)$, that is, one scaling factor f is applied to all values in the data set and this scale factor depends on the level, $f = f(L_i)$. This kind of scaling is commonly employed for vibrational frequencies (see Table 1). For intensities, however, we will see that approaches of the type $p(\text{exp}) \approx f \cdot p(L_i) + C(L_i)$ are more successful, that is, there will be a non-zero offset.

5.2. Scaling Approaches for the Computed Total Intensities of C–H Stretching Modes

Let $ML1$, $ML2$ and $ML3$ respectively represent the MP2(full) computations with the 6-31G*, 6-311+G(d,p), and 6-311+G(3df,3pd) basis sets [i.e., $ML1 \equiv \text{MP2}(\text{full})/6\text{-}31\text{G}^*$, $ML2 \equiv \text{MP2}(\text{full})/6\text{-}311\text{+G}(\text{d,p})$, and $ML3 \equiv \text{MP2}(\text{full})/6\text{-}311\text{+G}(\text{3df,3pd})$]. Let $BL1$, $BL2$ and $BL3$ respectively represent the B3LYP computations with the 6-31G*, 6-311+G(d,p), and 6-311+G(3df,3pd) basis sets (i.e., $BL1 \equiv \text{B3LYP}/6\text{-}31\text{G}^*$, $BL2 \equiv \text{B3LYP}/6\text{-}311\text{+G}(\text{d,p})$, and $BL3 \equiv \text{B3LYP}/6\text{-}311\text{+G}(\text{3df,3pd})$). As can be seen from Figure 9 (top left), the total intensities (A) computed at the MP2 level but with different basis sets [i.e., $A(ML1)$,

$A(ML2)$, and $A(ML3)$] are linearly related:

$$A(ML3) \approx 0.7615 A(ML1) , \quad (r^2 \approx 0.9575) \quad (1a)$$

$$A(ML3) \approx 0.9382 A(ML1) - 20.4880 , \quad (r^2 \approx 0.9949) \quad (1b)$$

$$A(ML3) \approx 0.8089 A(ML2) , \quad (r^2 \approx 0.9984) \quad (1c)$$

where r^2 is the linear-correlation coefficient. While eq. 1c describes an excellent linear correlation between the intensities computed with the $ML3$ method [$A(ML3)$] and that with the $ML2$ method [$A(ML2)$] without any need for an offset, the analogous eq. 1a is less successful and an excellent linear correlation between $A(ML3)$ and $A(ML1)$ only is achieved when a non-zero offset is allowed in eq. 1b. The analogous relations also hold at the B3LYP level (eq. 2) and they are shown in Figure 9 (top right), where $A(BL1)$, $A(BL2)$, and $A(BL3)$ are respectively the intensities computed at the $BL1$, $BL2$ and $BL3$ levels.

$$A(BL3) \approx 0.7306 A(BL1) , \quad (r^2 \approx 0.9610) \quad (2a)$$

$$A(BL3) \approx 0.8838 A(BL1) - 26.1670 , \quad (r^2 \approx 0.9924) \quad (2b)$$

$$A(BL3) \approx 0.8089 A(BL2) , \quad (r^2 \approx 0.9984) \quad (2c)$$

$$A(BL3) \approx 0.8395 A(BL2) - 3.3861 , \quad (r^2 \approx 0.9998) \quad (2d)$$

Also shown in Figure 9 (bottom left) are the nearly linear relations between the IR intensities computed at the B3LYP and MP2(full) levels with a common basis set. The data are very well described by linear regression and there is no need for a non-zero offset in any of the following equations (see eqs. 3a, 3b, and 3c). It is remarkable that these slopes are rather similar for the various basis sets.

$$A(ML1) \approx 0.6769 A(BL1) , \quad (r^2 \approx 0.9971) \quad (3a)$$

$$A(ML2) \approx 0.7877 A(BL2) , \quad (r^2 \approx 0.9966) \quad (3b)$$

$$A(ML3) \approx 0.7056 A(BL3) , \quad (r^2 \approx 0.9949) \quad (3c)$$

In light of these linear correlations, it is clear that there must be a strong linear correlation between the lowest DFT level, our standard level B3LYP/6-31G* (i.e., $BL1$), and the best MP2 level, the level MP2(full)/6-311+G(3df,3pd)

(i.e., *ML3*). Eqs. 1a and 3a suggest a proportionality constant of $\approx 0.7615 \times 0.6769 \approx 0.5154$ and the actual correlation coefficient of eq. 4a is ~ 0.5152 and it is essentially the same (see Figure 9, bottom right). Considering the need for non-zero offset in eq. 1b, we also explore eq. 4b and achieve an excellent linear correlation:

$$A(ML3) \approx 0.5152 A(BL1), \quad (r^2 \approx 0.9428) \quad (4a)$$

$$A(ML3) \approx 0.6655 A(BL1) - 25.6770, \quad (r^2 \approx 0.9964) \quad (4b)$$

We will demonstrate in the following that the offsets come from the fact that the intensities of methyl (aliphatic) and aromatic C–H stretches do not scale alike (i.e., $f_{\text{ali}} \neq f_{\text{aro}}$). Eqs. 5a and 5b show the total intensities of the C–H stretching regions as a function of the numbers of methyl ($n_{3.4}$) and aromatic ($n_{3.3}$) C–H bonds and the average IR intensities of a methyl ($A_{3.4}$) or of an aromatic ($A_{3.3}$) C–H stretching bond for two theoretical levels L_i and L_j :

$$A(L_i) = n_{3.4} A_{3.4}(L_i) + n_{3.3} A_{3.3}(L_i) \quad (5a)$$

$$A(L_j) = n_{3.4} A_{3.4}(L_j) + n_{3.3} A_{3.3}(L_j) \quad (5b)$$

where $A_{3.4}(L_i)$ and $A_{3.3}(L_i)$ are respectively the strengths of one aliphatic or one aromatic C–H bond computed at the L_i level, and $A_{3.4}(L_j)$ and $A_{3.3}(L_j)$ are the same parameters but computed at the L_j level.

Assuming that the intensities of the methyl (aliphatic) and aromatic C–H stretches scale with factors f_{ali} and f_{aro} , respectively, one can express the total intensity at level L_j as a function of the average IR intensities of a methyl (aliphatic) or of an aromatic C–H stretching bond at theoretical levels L_i [i.e., $A_{3.4}(L_i)$ and $A_{3.3}(L_i)$; see eq. 6a]. By addition and subtraction of the term $f_{\text{aro}} n_{3.4} A_{3.4}(L_i)$, it is possible to rewrite eq. 6a such that $A(L_j)$ is expressed as a function of $A(L_i)$ and $A_{3.4}(L_i)$ (see eq. 6d). Using instead the analogous term

$f_{\text{ali}} n_{3.3} A_{3.3}(L_i)$ gives $A(L_j)$ as a function of $A(L_i)$ and $A_{3.3}(L_i)$ (see eq. 7d).

$$A(L_j) = f_{\text{ali}} n_{3.4} A_{3.4}(L_i) + f_{\text{aro}} n_{3.3} A_{3.3}(L_i) \quad (6a)$$

$$= f_{\text{ali}} n_{3.4} A_{3.4}(L_i) + f_{\text{aro}} n_{3.3} A_{3.3}(L_i) + f_{\text{aro}} n_{3.4} A_{3.4}(L_i) - f_{\text{aro}} n_{3.4} A_{3.4}(L_i) \quad (6b)$$

$$= f_{\text{aro}} [n_{3.4} A_{3.4}(L_i) + n_{3.3} A_{3.3}(L_i)] + f_{\text{ali}} n_{3.4} A_{3.4}(L_i) - f_{\text{aro}} n_{3.4} A_{3.4}(L_i) \quad (6c)$$

$$= f_{\text{aro}} A(L_i) + \underline{(f_{\text{ali}} - f_{\text{aro}}) n_{3.4} A_{3.4}(L_i)} \quad (6d)$$

or

$$A(L_j) = f_{\text{ali}} n_{3.4} A_{3.4}(L_i) + f_{\text{aro}} n_{3.3} A_{3.3}(L_i) \quad (7a)$$

$$= f_{\text{ali}} n_{3.4} A_{3.4}(L_i) + f_{\text{aro}} n_{3.3} A_{3.3}(L_i) + f_{\text{ali}} n_{3.3} A_{3.3}(L_i) - f_{\text{ali}} n_{3.3} A_{3.3}(L_i) \quad (7b)$$

$$= f_{\text{aro}} [n_{3.4} A_{3.4}(L_i) + n_{3.3} A_{3.3}(L_i)] + f_{\text{aro}} n_{3.3} A_{3.3}(L_i) - f_{\text{ali}} n_{3.3} A_{3.3}(L_i) \quad (7c)$$

$$= f_{\text{ali}} A(L_i) + \underline{(f_{\text{aro}} - f_{\text{ali}}) n_{3.3} A_{3.3}(L_i)} \quad (7d)$$

where the underlined terms in eqs. 6d and 7d are responsible for the offset in the correlations between the total intensities at levels L_i and L_j , and these offsets vanish only when $f_{\text{aro}} = f_{\text{ali}}$. We will show in §5.3 that this condition never holds and, in addition, it also is not trivial to determine at what level f_{aro} and f_{ali} converge.

5.3. Theoretical Level Dependency of Intensity Scaling Factors f_{aro} and f_{ali} : Basis Set Effects at the B3LYP Level

The basis set effects were studied extensively at the B3LYP level for toluene and the three isomers of methylpyrene. The results are shown in Table 7 and illustrated in Figures 10 and 11.

The first observation is that $A_{3.3}$ is almost invariant to the specific nature of the molecule. The second observation is that there is a very large basis set dependency in that $A_{3.3}$ is greatly reduced with the improvements of the basis set.

A typical $A_{3,3}$ value at the B3LYP/6-31G* level is $\sim 18\text{--}20 \text{ km mol}^{-1}$ and this value drops to $\sim 12.5\text{--}13.3 \text{ km mol}^{-1}$, i.e., a scaling factor of $f_{\text{aro}} \approx 0.7$. In contrast, $A_{3,4}$ greatly depends on the specific isomer and the basis set dependency of $A_{3,4}$ is less than that of $A_{3,3}$. A typical $A_{3,4}$ value at the B3LYP/6-31G* level is $\sim 23\text{--}27 \text{ km mol}^{-1}$ and this value drops to $\sim 19\text{--}24 \text{ km mol}^{-1}$, i.e., a scaling factor of $f_{\text{ali}} \approx 0.85$.

The plots in Figure 10 (left) show that the absolute intensities are greatly improved by the addition of at least single sets of polarization functions on both C and H atoms (and larger sets of polarization functions provide only small additional benefits), by the presence of single sets of diffuse functions on carbons (while diffuse functions on H atoms are less important), and by replacing the split-valence basis set with a triply-split valence basis set. For our purposes the main question concerns the convergence of the intensity ratio $A_{3,4}/A_{3,3}$ as a function of the theoretical level. In this regard, the data suggest that an adequate convergence value is obtained even with split-valence basis sets and with single sets of diffuse function on carbons and single sets of polarization functions on all atoms (i.e., 6-31+G**, 6-311+G** or better).

The plots in Figure 10 (right) show the scaling factor of the levels B3LYP/ L_j relative to the intensity computed at the level B3LYP/6-311+G**; i.e., $A(L_j)/A(\text{B3LYP}/6\text{-}311\text{+G}^{**})$. As can be seen, for all of the levels L_j equal to or better than B3LYP/6-311+G** the scaling factors for the intensities of the methyl and aromatic C–H stretches are very similar. Figure 11 also shows that the band-strength ratios $A_{3,4}/A_{3,3}$ computed with the basis sets 6-311+G**, 6-311++G**, 6-311+G(3df,3pd), and 6-311++G(3df,3pd) have essentially reached the convergence limit. Meanwhile, as shown in Table 6, the $A_{3,4}/A_{3,3}$ is less dependent on the method than the basis sets. This is expected since the overall intensity calculated with different methods using a common basis set are linearly correlated (cf. eqs. 3). We therefore concluded that the B3LYP/6-311+G** method presents an excellent compromise between accuracy and computational demand.

Based on the insights derived from the above analysis, we decide to determine the structures of and to perform vibrational analyses for all parent systems and

all of their methyl-derivatives at the B3LYP/6-311+G** level so as to ensure reliable $A_{3.4}/A_{3.3}$ values. The energies and thermochemical parameters are listed in Table 4. The most important results of the vibrational analysis are summarized in Table 7.

6. Recommended Band Intensities

As shown in Figure 12 (top panel), the aromatic C–H stretch band strength does not vary significantly for different molecules. It has an average value (per aromatic C–H bond) of $\langle A_{3.3} \rangle \approx 14.03 \text{ km mol}^{-1}$, with a standard deviation of $\sigma(A_{3.3}) \approx 0.89 \text{ km mol}^{-1}$. On the other hand, the aliphatic C–H stretch band strength is more dependent on the nature of the molecule and also on the specific isomer. The average band strength (per aliphatic C–H bond) is $\langle A_{3.4} \rangle \approx 23.68 \text{ km mol}^{-1}$, and the standard deviation is $\sigma(A_{3.4}) \approx 2.48 \text{ km mol}^{-1}$.

All of the above values are calculated at the B3LYP/6-311+G** (i.e., *BL2*) level. As discussed in §5, these values need to be scaled. By taking MP2(full)/6-311+G(3df,3pd) (i.e., *ML3*) to be the level which gives the most reliable band strength, the intensities need to be scaled with two formulae: eqs. 1c and 3b. Thus, we recommend the value of $\langle A_{3.3} \rangle \approx 14.03 \times 0.7877 \times 0.8089 \approx 8.94 \text{ km mol}^{-1}$ (i.e., $\sim 1.49 \times 10^{-18} \text{ cm}$ per C–H bond), and $\langle A_{3.4} \rangle \approx 23.68 \times 0.7877 \times 0.8089 \approx 15.09 \text{ km mol}^{-1}$ (i.e., $\sim 2.50 \times 10^{-18} \text{ cm}$ per C–H bond).

For the $A_{3.4}/A_{3.3}$ ratio, we have shown in §5.3 that the B3LYP/6-311+G** level provides reliable values. In Figure 12 (bottom panel) we show the $A_{3.4}/A_{3.3}$ ratio calculated at this level. We see that for all the molecules considered in this work the $A_{3.4}/A_{3.3}$ values fall in the range between ~ 1.4 and ~ 2.3 , with an average value of $\langle A_{3.4}/A_{3.3} \rangle \approx 1.76$.¹² Considering that $A_{3.4}$ depends significantly on the specific molecule and isomers while $A_{3.3}$ is relatively stable for all the molecules, it is not surprising that the $A_{3.4}/A_{3.3}$ values show a high structure dependency. For example, as shown in Table 8, the methyl group of

¹²From the mean band strengths $\langle A_{3.3} \rangle \approx 8.94 \text{ km mol}^{-1}$ and $\langle A_{3.4} \rangle \approx 15.09 \text{ km mol}^{-1}$ we obtain $\langle A_{3.4} \rangle / \langle A_{3.3} \rangle \approx 1.69$.

the five phenanthrene isomers give rise to $A_{3.4}/A_{3.3}$ between ~ 1.4 and ~ 1.9 . A similar isomer dependency is observed for perylene with $A_{3.4}/A_{3.3}$ between ~ 1.5 and ~ 2.2 . It is important to fully realize this high structure-dependency of the $A_{3.4}/A_{3.3}$ ratio and this finding stresses the need to study the formation processes for methyl-substituted PAHs.

Finally, we also show in Table 8 the experimental $A_{3.4}/A_{3.3}$ values obtained from the NIST absorption spectra, $(A_{3.4}/A_{3.3})_{\text{NIST}}$.

7. Astrophysical Implications

In some HII regions, reflection nebulae and planetary nebulae (as well as extragalactic regions, e.g., see Yamagishi et al. 2012, Kondo et al. 2012, Kaneda et al. 2014), the UIE band near $3\ \mu\text{m}$ exhibits a rich spectrum: the dominant $3.3\ \mu\text{m}$ feature is usually accompanied by a weaker feature at $3.4\ \mu\text{m}$ along with an underlying plateau extending out to $\sim 3.6\ \mu\text{m}$ (see Figure 2). In some objects, a series of weaker features at 3.46 , 3.51 , and $3.56\ \mu\text{m}$ are also seen superimposed on the plateau, showing a tendency to decrease in strength with increasing wavelength (see Geballe et al. 1985, Jourdain de Muizon et al. 1986, Joblin et al. 1996). While the assignment of the $3.3\ \mu\text{m}$ emission feature to the aromatic C–H stretch is widely accepted, the precise identification of the $3.4\ \mu\text{m}$ feature (and the accompanying weak features at 3.46 , 3.51 , and $3.56\ \mu\text{m}$ and the broad plateau) remains somewhat controversial. By assigning the $3.4\ \mu\text{m}$ emission exclusively to aliphatic C–H, one can place an upper limit on the aliphatic fraction of the emitters of the UIE features.

Let $I_{3.4}$ and $I_{3.3}$ respectively be the observed intensities of the $3.4\ \mu\text{m}$ and $3.3\ \mu\text{m}$ emission features. Let $N_{\text{H,aliph}}$ and $N_{\text{H,arom}}$ respectively be the numbers of aliphatic and aromatic C–H bonds in the emitters of the $3.3\ \mu\text{m}$ UIE feature. We obtain $N_{\text{H,aliph}}/N_{\text{H,arom}} \approx (I_{3.4}/I_{3.3}) \times (A_{3.3}/A_{3.4})$. We assume that one aliphatic C atom corresponds to 2.5 aliphatic C–H bonds (intermediate between methylene $-\text{CH}_2$ and methyl $-\text{CH}_3$) and one aromatic C atom corresponds to 0.75 aromatic C–H bond (intermediate between benzene C_6H_6

and coronene C₂₄H₁₂). Therefore, in the UIE carriers the ratio of the number of C atoms in aliphatic units to that in aromatic rings is $N_{\text{C,aliph}}/N_{\text{C,arom}} \approx (0.75/2.5) \times N_{\text{H,aliph}}/N_{\text{H,arom}} = 0.3 \times (I_{3.4}/I_{3.3}) \times (A_{3.3}/A_{3.4})$. Yang et al. (2013) have compiled and analyzed the UIE spectra of 35 sources available in the literature which exhibit both the 3.3 μm and 3.4 μm C–H features. They derived a median ratio of $\langle I_{3.4}/I_{3.3} \rangle \approx 0.12$, with the majority (31/35) of these sources having $I_{3.4}/I_{3.3} < 0.25$ (see Figure 15). With an average bond strength ratio of $A_{3.4}/A_{3.3} \approx 1.76$ (see §6), we obtain $N_{\text{C,aliph}}/N_{\text{C,arom}} \approx 0.02$. This suggests that the UIE emitters are predominantly aromatic and the aliphatic component is only a very minor part of the UIE emitters.

So far we have been focusing on the mono-methyl derivatives of selected, relatively small PAHs. In reality, one would assume that the PAH molecules in space cover a much larger range of sizes, from a few tens of C atoms up to several thousands, with a mean size of ~ 100 C atoms (see Li & Draine 2001). They may include defects, substituents (e.g., N in place of C; see Hudgins et al. 2005), partial dehydrogenation, and sometimes superhydrogenation. They could also include larger alkyl side chains (ethyl, propyl, butyl, ...), and several alkyl side chains might be present in one PAH molecule. Moreover, the alkyl side chains and spacers might be unsaturated (i.e., $-\text{CH}=\text{CH}_2$, $-\text{CH}=\text{CH}-$, $\text{C}=\text{CH}_2$, $\text{C}=\text{C}-\text{H}$). Kwok & Zhang (2013) argued that the 3.4 μm interstellar emission feature may not be the only manifestation of the aliphatic structures of the UIE emitters. They hypothesized that the clustering of aromatic rings may break up the simple methyl- or methylene-like side groups and hence the aliphatic components may take many other forms.

Considering that many functional groups other than methyl might also attach to the aromatic rings and arise a feature at 3.4 μm , we also included them in our computations (see Yang et al. 2016a for details). These computations were performed at B3LYP/6-311+G**, our standard level. The structures considered are shown in Figure 13 and they cover a wide range of sidegroups, including ethyl ($-\text{CH}_2-\text{CH}_3$), propyl ($-\text{CH}_2-\text{CH}_2-\text{CH}_3$), butyl ($-\text{CH}_2-\text{CH}_2-\text{CH}_2-\text{CH}_3$), and several unsaturated alkyl groups and spacers ($-\text{CH}=\text{CH}_2$, $-\text{CH}=\text{CH}-$

, C=CH₂, C=C-H).

From the top panel of Figure 16, we can see that the aliphatic C-H stretch band strength varies within a wide range. For ethyl, propyl and butyl, the values ($\sim 25\text{--}30 \text{ km mol}^{-1}$) are generally consistent with methyl (c.f. Figure 12 top panel), while those for the unsaturated alkyl chains (-CH=CH₂, -CH=CH-, C=CH₂, C=C-H) are much lower ($\sim 5\text{--}15 \text{ km mol}^{-1}$). On the other hand, the aromatic C-H stretch band strength stays stable for all the groups, $\sim 10\text{--}15 \text{ km mol}^{-1}$, which is also consistent with the corresponding value of methyl PAHs (c.f. Figure 12 top panel). Therefore, we conclude that the $A_{3.4}/A_{3.3}$ ratios for PAHs with ethyl, propyl and butyl groups are close to that of methyl PAHs. The $A_{3.4}/A_{3.3}$ ratios for PAHs with unsaturated alkyl chains could be lower by a factor of up to ~ 3 than that of methyl PAHs. However, it is apparent that PAHs with unsaturated alkyl chains are less stable than methyl PAHs when subject to UV photons in the ISM. We also note that PAHs with a large side chain are not as stable against photolytic dissociation as methyl-substituted PAHs. If a large aliphatic chain (e.g., -CH₂-CH₃) is attached to an aromatic structure, the most likely photodissociation product is a benzyl radical PAH- $\dot{\text{C}}\text{H}_2$ (i.e., a -CH₂ group attached to a PAH molecule), which, when subject to the reaction PAH- $\dot{\text{C}}\text{H}_2 + \text{H} \rightarrow \text{PAH-CH}_3$ will rapidly lead to the product of a CH₃ group at the periphery of an aromatic molecule (Joblin et al. 1996; Hwang et al. 2002). Therefore, neither PAHs with a large side chain nor PAHs with unsaturated alkyl chains are expected to be present in the ISM in a large abundance.

Considering that several alkyl side chains might be present in one PAH molecule, we also consider the situation that there are two methyl groups attached to a PAH molecule, using pyrene as an example (see Yang et al. 2016a for details). We consider all possible isomers of dimethyl-substituted pyrene (see Figure 17). For dimethyl pyrenes, the aliphatic C-H stretch band strength varies within $\sim 18\text{--}27 \text{ km mol}^{-1}$, while these values for the aromatic C-H stretch are generally $\sim 15 \text{ km mol}^{-1}$ (c.f. Figure 18 top panel). The $A_{3.4}/A_{3.3}$ ratios vary from ~ 1.25 (Pyre110) to ~ 1.75 (Pyre27), with an average ratio of

$\langle A_{3.4}/A_{3.3} \rangle \approx 1.57$ (c.f. Figure 18 bottom panel), which is only $\sim 11\%$ lower than the mean ratio of $\langle A_{3.4}/A_{3.3} \rangle \approx 1.76$ computed from methyl PAHs (see §6).

The methyl groups are essentially independent of each other. Noticeable effects on frequency and intensity only occur when several alkyl groups are placed in direct proximity. We note that for methyl PAHs the frequencies of the aliphatic C–H stretch are always smaller than $\sim 3000 \text{ cm}^{-1}$ and those for the aromatic C–H stretch are larger than $\sim 3000 \text{ cm}^{-1}$. The positions of the C–H stretches of simple alkenes and dienes coincide with the methyl signals of methyl-substituted PAHs. However, for $\text{CH}=\text{CH}_2$ and $\text{C}=\text{CH}_2$, one of the aliphatic C–H stretches falls at $\sim 3120 \text{ cm}^{-1}$ (i.e. in the “aromatic” region). For dimethyl pyrene Pyre45, there is also one frequency of the aliphatic C–H stretches that falls in the “aromatic” region ($\sim 3070 \text{ cm}^{-1}$).

One may argue that the aliphatic chains and aromatic rings in the MAON-, coal-, or kerogen-like UIE carriers may cluster together and not every C atom is bonded to H atoms, and therefore the C–H bands may not fully reveal the aliphatic C. We note that the clustering of aromatic rings and aliphatic chains would be accompanied by forming new C=C bonds and losing H atoms. Laboratory measurements have also shown that the reduction of H atoms leads to aromatization: with decreasing H/C and O/C ratios, coal-like solid hydrocarbon materials become more aromatic and exhibit weaker aliphatic $3.4 \mu\text{m}$ features and stronger $3.3 \mu\text{m}$ aromatic feature (Papoular et al. 1989).

Finally, we note that, in addition to the $3.4 \mu\text{m}$ C–H stretching mode, aliphatic hydrocarbon materials also have two C–H deformation bands at $6.85 \mu\text{m}$ and $7.25 \mu\text{m}$. These two bands have been observed in weak *absorption* in the Galactic diffuse ISM (Chiar et al. 2000). They are also seen in *emission*, with the $6.85 \mu\text{m}$ feature detected both in the Milky Way and in the Large and Small Magellanic Clouds while the $7.25 \mu\text{m}$ feature so far mostly seen in the Magellanic Clouds (e.g., see Sloan et al. 2014). Their strengths (relative to the nearby 6.2 and $7.7 \mu\text{m}$ C–C stretching bands) also allow an estimate of the aliphatic fraction of the UIE carrier. We have explored the aliphatic versus aromatic con-

tent of the UIE carriers by examining the ratio of the observed intensity of the $6.2\ \mu\text{m}$ aromatic C–C feature to that of the $6.85\ \mu\text{m}$ aliphatic C–H deformation features. The fraction of C atoms in aliphatic form was derived to be at most $\sim 10\%$, confirming that the UIE emitters are predominantly aromatic (see Yang et al. 2016b).

8. Summary

The UIE carriers play an essential role in astrophysics as an absorber of the UV starlight, as an agent for photoelectrically heating the interstellar gas, and as a valid indicator of the cosmic star-formation rates. While the exact nature of the UIE carriers remains unknown, the ratios of the observed intensities of the $3.3\ \mu\text{m}$ aromatic C–H stretching emission feature ($I_{3.3}$) to that of the $3.4\ \mu\text{m}$ aliphatic C–H emission feature ($I_{3.4}$) could provide constraints on the chemical structures of the UIE carriers, i.e., are they mainly aromatic or largely aliphatic with a mixed aromatic/aliphatic structure? To this end, the knowledge of the intrinsic strengths (per chemical bond) of the $3.3\ \mu\text{m}$ aromatic C–H stretch ($A_{3.3}$) and the $3.4\ \mu\text{m}$ aliphatic C–H stretch ($A_{3.4}$) is required. It is the purpose of this review to present an overview on how $A_{3.4}/A_{3.3}$ is derived from extensive computations of the vibrational frequencies and intensities of a range of methyl PAHs and PAHs with other side groups, using density functional theory and second-order perturbation theory to compute their vibrational spectra. The major results are:

1. The structures and excitation mechanisms of the major proposed carriers are examined in terms of two broad categories: free-flying PAH molecules or solid hydrocarbon materials with a mixed aromatic/aliphatic structure (HAC, QCC, soot, coal/kerogen, MAON).
2. The hybrid density functional theoretical method (B3LYP) in conjunction with a variety of basis sets [6-31G*, 6-31+G*, 6-311+G*, 6-311G**, 6-31+G**, 6-31++G**, 6-311+G**, 6-311++G**, 6-311+G(3df,3pd), and 6-311++G(3df,3pd)] are employed to calculate the vibrational spectra

for a range of aromatic molecules (naphthalene, anthracene, phenanthrene, pyrene, perylene, and coronene) with a methyl side chain. Møller-Plesset perturbation theory (MP2) is also included with basis sets 6-311+G** and 6-311++G(3df,3pd) for some of the molecules.

3. With the use of the standard frequency scale factors, a good to excellent agreement between the measured and computed C–H stretch vibrational frequencies is achieved in all cases, for all molecules at all levels.
4. The band intensities calculated with B3LYP/6-31G* are much higher than the gas-phase experimental values. Using better basis sets in conjunction with the B3LYP method, the computed intensities are still considerably higher (by $\sim 30\%$) compared to the experimental results.
5. The MP2(full) method with the basis set of 6-311+G(3df,3pd) reproduces the measured intensities reasonably well. However, such calculations are far too expensive especially for large molecules. It is shown that intensity scaling approaches that are based on the B3LYP data can be just as successful.
6. By taking MP2(full)/6-311+G(3df,3pd) to be the level which gives the most reliable band strengths, we determine and apply scaling factors to the intensities computed at the B3LYP/6-311+G** level. The recommended band strengths (per chemical bond) are $\langle A_{3,3} \rangle \approx 8.94 \text{ km mol}^{-1}$ (i.e., $\sim 1.49 \times 10^{-18} \text{ cm}$ per C–H bond), and $\langle A_{3,4} \rangle \approx 15.09 \text{ km mol}^{-1}$ (i.e., $\sim 2.50 \times 10^{-18} \text{ cm}$ per C–H bond), where $A_{3,4}$ depends significantly on the specific molecule and isomers while $A_{3,3}$ is relatively stable for all the molecules.
7. The band-strength ratios $A_{3,4}/A_{3,3}$ computed with the basis sets 6-311+G**, 6-311++G**, 6-311+G(3df,3pd), and 6-311++G(3df,3pd) essentially reach the convergence limit. The $A_{3,4}/A_{3,3}$ ratio is less dependent on the method than the basis sets. The B3LYP/6-311+G** method presents an excellent compromise between accuracy and computational demand. Therefore, to ensure reliable $A_{3,4}/A_{3,3}$ values, we adopt this theoretical level to compute all of the molecules. For the molecules considered in this work the

$A_{3.4}/A_{3.3}$ values fall in the range between ~ 1.4 and ~ 2.3 , with an average value of $\langle A_{3.4}/A_{3.3} \rangle \approx 1.76$.

8. By attributing the $3.4 \mu\text{m}$ feature exclusively to aliphatic C–H stretch (i.e., neglecting anharmonicity and superhydrogenation), we derive the fraction of C atoms in aliphatic form from $I_{3.4}/I_{3.3} \approx 0.12$ and $A_{3.4}/A_{3.3} \approx 1.76$ to be $\sim 2\%$, where $I_{3.4}/I_{3.3}$, the ratio of the power emitted from the $3.4 \mu\text{m}$ feature to that from the $3.3 \mu\text{m}$ feature, has a median ratio of $\langle I_{3.4}/I_{3.3} \rangle \approx 0.12$ for 35 astronomical sources which exhibit both the $3.3 \mu\text{m}$ and $3.4 \mu\text{m}$ C–H features. We conclude that the UIE emitters are predominantly aromatic.
9. Dimethyl pyrene is studied in the context that several alkyl side chains might be present in one PAH molecule. The $A_{3.4}/A_{3.3}$ ratio averaged over all the isomers of dimethyl-substituted pyrene is ~ 1.57 , which is only $\sim 11\%$ lower than that of mono-methyl PAHs.
10. A wide range of sidegroups (other than methyl and dimethyl) have also been considered, including ethyl ($-\text{CH}_2-\text{CH}_3$), propyl ($-\text{CH}_2-\text{CH}_2-\text{CH}_3$), butyl ($-\text{CH}_2-\text{CH}_2-\text{CH}_2-\text{CH}_3$) and several unsaturated alkyl chains ($-\text{CH}=\text{CH}_2$, $-\text{CH}=\text{CH}-$, $\text{C}=\text{CH}_2$, $\text{C}=\text{C}-\text{H}$). The corresponding $A_{3.4}/A_{3.3}$ ratios are close to that of mono-methyl PAHs, except PAHs with unsaturated alkyl chains (for which the $A_{3.4}/A_{3.3}$ ratios could be lower by a factor of up to ~ 3). However, these molecules are photolytically less stable compared to methyl PAHs and are not expected to be present in the ISM in a large abundance. The aliphatic C–H stretches of PAHs with unsaturated alkyl chains often fall in the wavelength range even shortward of the aromatic C–H stretch which are not seen in the ISM.

Acknowledgements

We thank Dr. T.J. Horscroft and Prof. S.N. Zhang for inviting us to submit this review and also for their support and patience during the preparation of this review. We thank Prof. B.T. Draine, Dr. J.Y. Seok, and the anonymous

referee for very helpful suggestions. AL and XJY are supported in part by NSFC 11473023, NSFC 11273022, NSF AST-1311804, NNX13AE63G, Hunan Provincial NSF 2015JJ3124, and the University of Missouri Research Board. RG is supported in part by NSF-PRISM grant Mathematics and Life Sciences (0928053). Computations were performed using the high-performance computer resources of the University of Missouri Bioinformatics Consortium.

References

- [1] Allamandola, L.J., Tielens, A.G.G.M., & Barker, J.R. 1985, *ApJ*, 290, L25
- [2] Allamandola, L.J., Tielens, A.G.G.M., & Barker, J.R. 1989, *ApJS*, 71, 733
- [3] Allamandola, L.J., Hudgins, D.M., & Sandford, S.A. 1999, *ApJ*, 511, 115
- [4] Andersson, M. P., Blomquist, J., & Uvdal, P. 2005, *J. Chem. Phys.*, 123, 224714
- [5] Balm, S. P., & Kroto, H. W. 1990, *MNRAS*, 245, 193
- [6] Barker, J.R., Allamandola, L.J., & Tielens, A.G.G.M. 1987, *ApJ*, 315, L61
- [7] Bakes, E. L. O., & Tielens, A. G. G. M. 1994, *ApJ*, 427, 822
- [8] Bauschlicher, C. W., Jr., Liu, Y., Ricca, A., Mattioda, A. L., & Allamandola, L. J. 2007, *ApJ*, 671, 458
- [9] Bauschlicher, C. W., Jr., Boersma, C., Ricca, A., et al. 2010, *ApJS*, 189, 341
- [10] Bernstein, M.P., Sandford, S.A., & Allamandola, L.J. 1996, *ApJ*, 472, L127
- [11] Bertie, J. E., & Keefe, C. D. 1994, *J. Chem. Phys.*, 101, 4610
- [12] Borowski, P. 2012, *J. Phys. Chem. A*, 116, 3866
- [13] Calzetti, D. 2011, *EAS Publ. Ser.*, Vol.46, PAHs and the Universe: A Symposium to Celebrate the 25th Anniversary of the PAH Hypothesis, ed. J.-P. Zahn (Cambridge: Cambridge Univ. Press), 133

- [14] Cami, J., Bernard-Salas, J., Peeters, E., & Malek, S. E. 2010, *Science*, 329, 1180
- [15] Cané E., Palmieri P., Tarroni R., Trombetti A., & Handy N. C. 1996, *Gazz. Chim. Ital.*, 126, 289
- [16] Cané E., Miani A., Palmieri P., Tarroni R., & Trombetti A. 1997, *J. Chem. Phys.*, 106, 9004
- [17] Cataldo, F., García-Hernández, D. A., & Manchado, A. 2013, *MNRAS*, 429, 3025
- [18] Cecchi-Pestellini, C., Malloci, G., Mulas, G., Joblin, C., & Williams, D. A. 2008, *A&A*, 486, L25
- [19] Chiar, J.E., Tielens, A.G.G.M., Whittet, D.C.B., et al. 2000, *ApJ*, 537, 749
- [20] Chiar, J. E., Tielens, A. G. G. M., Adamson, A. J., & Ricca, A. 2013, *ApJ*, 770, 78
- [21] Dartois, E., Geballe, T.R., Pino, T., et al. 2007, *A&A*, 463, 635
- [22] Draine, B.T., & Li, A. 2001, *ApJ*, 551, 807
- [23] Draine, B.T., & Li, A. 2007, *ApJ*, 657, 810
- [24] Duley, W. W., Jones, A. P., & Williams, D. A. 1989, *MNRAS*, 236, 709
- [25] Duley, W.W., & Williams, D.A. 1981, *MNRAS*, 196, 269
- [26] Duley, W. W., & Williams, D. A. 1988, *MNRAS*, 231, 969
- [27] Frisch, M. J., Trucks, G. W., Schlegel, H. B., et al. 2009, *Gaussian 09, Revision B01*, Gaussian, Inc., Wallingford CT
- [28] Galabov., B., Ilieva, S., Gounev., T., & Steele, D. 1992, *J. Mol. Struct.*, 273, 85
- [29] Geballe, T.R., Lacy, J.H., Persson, S.E., McGregor, P.J., & Soifer, B.T. 1985, *ApJ*, 292, 500

- [30] Geballe, T. R., Tielens, A. G. G. M., Kwok, S., & Hrivnak, B. J. 1992, *ApJL*, 387, L89
- [31] Gillett, F.C., Forrest, W.J., & Merrill, K.M. 1973, *ApJ*, 183, 87 1985, *ApJ*, 292, 500
- [32] Herzberg, H. 1945, *Molecular Spectra and Molecular Structure II: Infrared and Raman Spectra of Polyatomic Molecules*. Van Nostrand: Princeton, New Jersey, p. 365
- [33] Hudgins, D. M., Bauschlicher, C. W., Jr., & Allamandola, L. J. 2005, *ApJ*, 632, 316
- [34] Joblin, C., Léger, A., & Martin, P. 1992, *ApJ*, 393, L79
- [35] Joblin C., d'Hendecourt L., Léger A., & Defourneau, D. 1994, *A&A*, 281, 923
- [36] Joblin, C., Tielens, A.G.G.M., Allamandola, L.J., & Geballe, T.R. 1996, *ApJ*, 458, 610
- [37] Jones, A. P., Duley, W. W., & Williams, D.A. 1990, *QJRAS*, 31, 567
- [38] Jones, A. P., Fanciullo, L., Köhler, M., et al. 2013, *A&A*, 558, A62
- [39] Jourdain de Muizon, M., Geballe, T.R., d'Hendecourt, L.B., & Baas, F. 1986, *ApJ*, 306, L105
- [40] Hwang, C.L., Jiang, J.C., Lee, Y.T., & Ni, C.K. 2002, *J. Chem. Phys.*, 117, 15
- [41] Kaneda, H., Ishihara, D., Kobata, K., et al. 2014, *Planet. Space Sci.*, 100, 6
- [42] Kondo, T., Kaneda, H., Oyabu, S., et al. 2012, *ApJ*, 751, L18
- [43] Kwok, S., & Zhang, Y. 2011, *Nature*, 479, 80
- [44] Kwok, S., & Zhang, Y. 2013, *ApJ*, 771, 5

- [45] Léger, A., & Puget, J. 1984, *A&A*, 137, L5
- [46] Li, A., 2004, in *Astrophysics of Dust*, Witt, A.N., Clayton, G.C., & Draine, B.T. (eds.), *ASP Conf. Ser.*, 309, 417
- [47] Li, A., & Draine, B.T. 2001, *ApJ*, 554, 778
- [48] Li, A., & Draine, B.T. 2002, *ApJ*, 572, 232
- [49] Li, A., & Draine, B.T. 2012, *ApJ*, 760, L35
- [50] Lepp, S., & Dalgarno, A. 1988, *ApJ*, 335, L769
- [51] Merrick, J.P., Moran, D., & Radom, L. 2007, *J. Phys. Chem. A*, 111, 11683
- [52] Mitra, S. S., & Bernstein, H. J. 1959, *Can. J. Chem.*, 37, 553
- [53] Mori, T. I., Onaka, T., Sakon, I., et al. 2014, *ApJ*, 784, 53
- [54] Mulas, G., Zonca, A., Casu, S., & Cecchi-Pestellini, C. 2013, *ApJS*, 207, 7
- [55] Nagata, T., Tokunaga, A. T., Sellgren, K., et al. 1988, *ApJ*, 326, 157
- [56] Papoular, R., Conrad, J., Giuliano, M., Kister, J., & Mille, G. 1989, *A&A*, 217, 204
- [57] Papoular, R. 2001, *A&A*, 378, 597
- [58] Pauzat, F., Talbi, D., & Ellinger, Y. 1999, *MNRAS*, 304, 241
- [59] Pavlyuchko, A.I., Vasilyev, E.V. & Gribov, L.A. 2012, *J. Appl. Spectrosc.*, 78, 782
- [60] Peeters, E. 2011, *IAU Symp. 280, The Molecular Universe*, ed. J. Cernicharo & R. Bachiller (Cambridge: Cambridge Univ. Press), 149
- [61] Peeters, E., Allamandola, L.J., Hudgins, D.M., Hony, S., & Tielens, A.G.G.M. 2004, in *Astrophysics of Dust (ASP Conf. Ser. 309)*, ed. A.N. Witt, G.C. Clayton, & B.T. Draine (San Francisco, CA: ASP), 141

- [62] Peeters, E., Spoon, H. W. W., & Tielens, A. G. G. M. 2004, *ApJ*, 613, 986
- [63] Pendleton, Y.J., & Allamandola, L.J. 2002, *ApJS*, 138, 75
- [64] Ricca, A., Bauschlicher, C. W., Jr., Boersma, C., Tielens, A. G. G. M., & Allamandola, L. J. 2012, *ApJ*, 754, 75
- [65] Riechers, D. A., Pope, A., Daddi, E., et al. 2014, *ApJ*, 796, 84
- [66] Robertson, J. 1986, *Adv. Phys.*, 35, 317
- [67] Rouillé, G., Steglich, M., Carpentier, Y., et al. 2012, *ApJ*, 752, 25
- [68] Sakata, A., Wada, S., Onaka, T., & Tokunaga, A. T. 1990, *ApJS*, 353, 543
- [69] Salama, F., et al. 2011, *ApJ*, 728, 154
- [70] Sandford, S. A. 1991, *ApJ*, 376, 599
- [71] Sandford, S. A., Bernstein, M. P., & Materese, C. K. 2013, *ApJS*, 205, 8
- [72] Sellgren, K., Werner, M. W., & Dinerstein, H. L. 1983, *ApJ*, 271, L13
- [73] Sellgren, K. 1984, *ApJ*, 277, 623
- [74] Sellgren, K., Werner, M. W., Ingalls, J. G., et al. 2010, *ApJ*, 722, L54
- [75] Sloan, G.C., Bregman, J.D., Geballe, T.R., Allamandola, L.J., & Woodward, C.E. 1997, *ApJ*, 474, 735
- [76] Sloan, G. C., Jura, M., Duley, W. W., et al. 2007, *ApJ*, 664, 1144
- [77] Sloan, G. C., Lagadec, E., Zijlstra, A. A., et al. 2014, *ApJ*, 791, 28
- [78] Smith, J. D. T., Draine, B. T., Dale, D. A., Moustakas, J., et al. 2007, *ApJS*, 656, 770
- [79] Smith, T. L., Clayton, G. C., & Valencic, L. 2004, *AJ*, 128, 357
- [80] Steglich, M., Jäger, C., Rouillé, G., Huisken, F., Mutschke, H., & Henning, T. 2010, *ApJ*, 712, L16

- [81] Steglich, M., Jäger, C., Huisken, F., et al. 2013, *ApJS*, 208, 26
- [82] Tielens, A. G. G. M. 1990, in *Carbon in the Galaxy: Studies from Earth and Space*, ed. J. C. Tarter, S. Chang, & D. J. DeFrees (Washington: NASA), 59
- [83] Tielens, A. G. G. M. 2008, *ARA&A*, 46, 289
- [84] Verstraete, L., Léger, A., D'Hendecourt, L., Defourneau, D., & Dutuit, O. 1990, *A&A*, 237, 436
- [85] Verstraete, L. 2011, *EAS Publ. Ser.*, Vol. 46, *PAHs and the Universe: A Symposium to Celebrate the 25th Anniversary of the PAH Hypothesis*, ed. J.-P. Zahn (Cambridge: Cambridge Univ. Press), 415
- [86] Vijh, U. P., Witt, A. N., & Gordon, K. D. 2005, *ApJ*, 619, 368
- [87] Vijh, U. P., Witt, A. N., & Gordon, K. D. 2005, *ApJ*, 633, 262
- [88] Wagner, D.R., Kim, H., & Saykally, R.J. 2000, *ApJ*, 545, 854
- [89] Wilshurst, J. K. & Bernstein, H. J. 1957, *Can. J. Chem.*, 35, 911
- [90] Weingartner, J. C., & Draine, B. T. 2001, *ApJS*, 134, 263
- [91] Witt, A.N. 2014, in *IAU Symp. 297, Diffuse Interstellar Bands*, ed. J. Cami, & N. Cox (Cambridge: Cambridge Univ. Press), 173
- [92] Yamagishi, M., Kaneda, H., Ishihara, D., et al. 2012, *A&A*, 541, A10
- [93] Yang, X. J., Glaser, R., Li, A., & Zhong, J. X. 2013, *ApJ*, 776, 110
- [94] Yang, X. J., Li, A., Glaser, R., & Zhong, J. X. 2016a, *ApJ*, 825, 22
- [95] Yang, X. J., Glaser, R., Li, A., & Zhong, J. X. 2016b, *MNRAS*, 462, 1551
- [96] Yang, X. J., Li, A., Glaser, R., & Zhong, J. X. 2017, *ApJ*, in press (arXiv:1702.02487)

Proposed Carriers for the “Unidentified Infrared” Emission Features

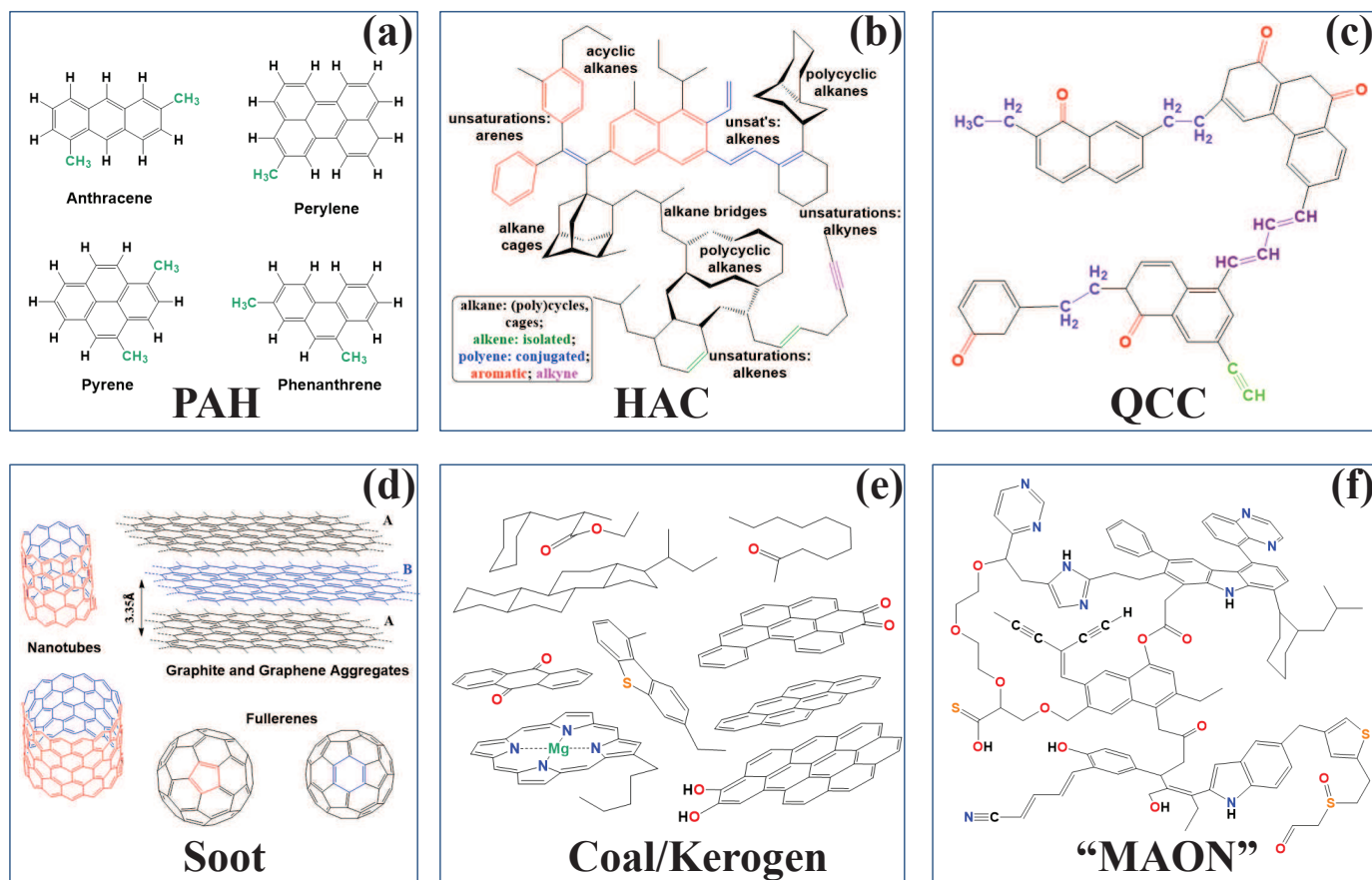


Figure 1: Schematic structures for the possible UIE carriers: (a) free-flying PAHs, (b) bulk HAC, (c) bulk QCC, (d) bulk soot, (e) bulk coal or kerogen, and (f) nano MAONs (“mixed aromatic/aliphatic organic nanoparticles”).

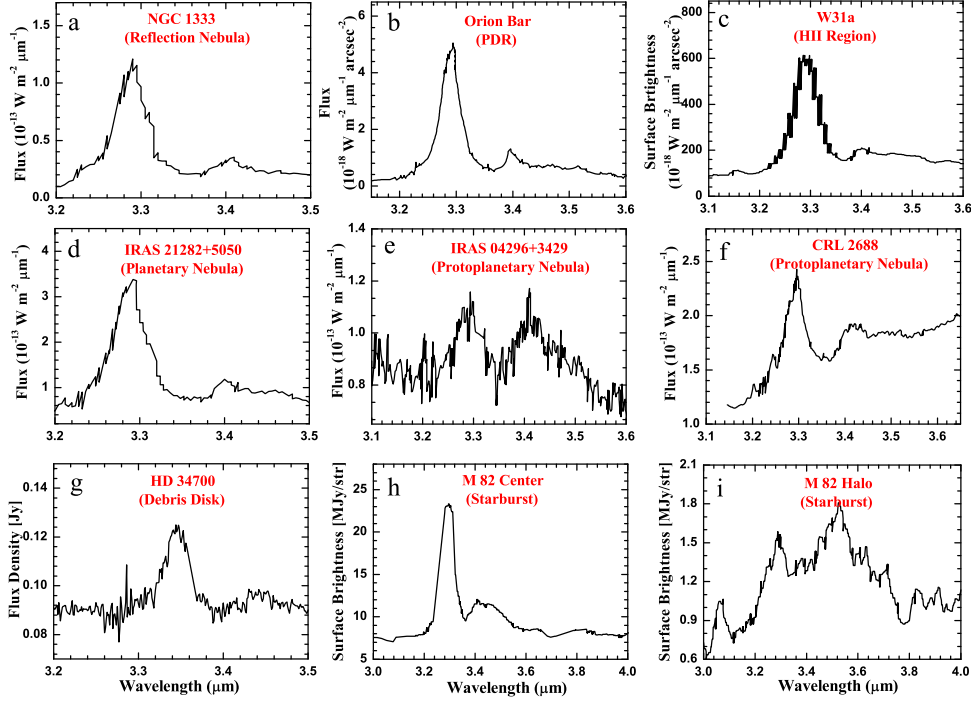


Figure 2: Aromatic and aliphatic C–H stretching emission features seen in representative astrophysical regions: (a) NGC 1333 (reflection nebula, Joblin et al. 1996), (b) Orion bar (photodissociation region [PDR], Sloan et al. 1997), (c) W31a (HII region, Mori et al. 2014), (d) IRAS 21282+5050 (planetary nebula, Nagata et al. 1988), (e) IRAS 04296+3429 (protoplanetary nebula, Geballe et al. 1992), (f) CRL 2688 (protoplanetary nebula, Geballe et al. 1992), (g) HD 34700 (debris disk, Smith et al. 2004), (h) M82 center (starburst galaxy, Yamagishi et al. 2012), and (i) M82 halo (Yamagishi et al. 2012).

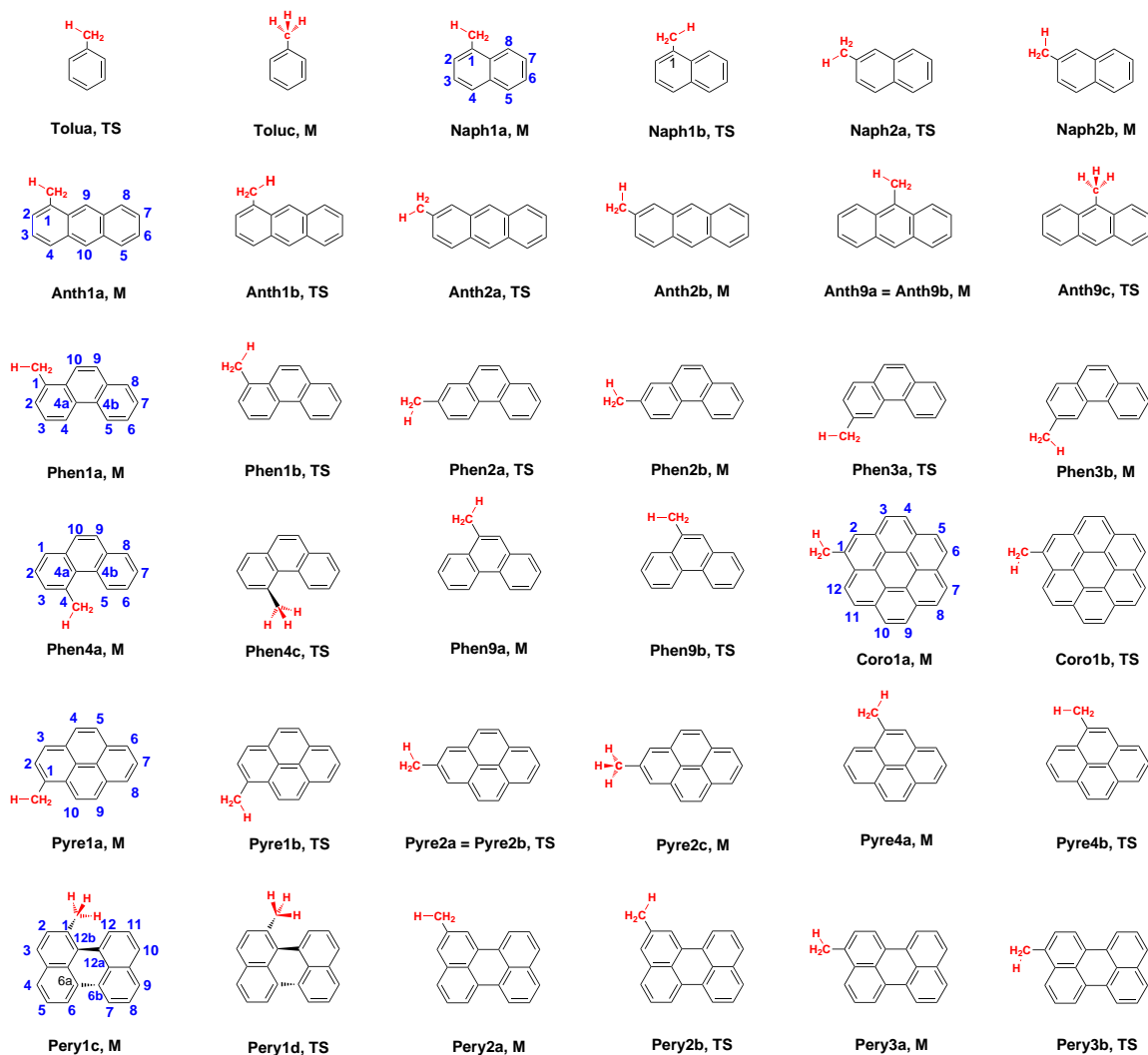


Figure 3: Structures of the mono-methyl ($-\text{CH}_3$) derivatives of seven aromatic molecules together with the standard IUPAC numbering: benzene (C_6H_6), naphthalene (C_{10}H_8), anthracene ($\text{C}_{14}\text{H}_{10}$), phenanthrene ($\text{C}_{14}\text{H}_{10}$), pyrene ($\text{C}_{16}\text{H}_{10}$), perylene ($\text{C}_{20}\text{H}_{12}$), and coronene ($\text{C}_{24}\text{H}_{12}$). We use the first four letters of the parent molecules to refer to them and attach the position number of the location of the methyl group (e.g., Naph1 for 1-methylnaphthalene). The mono-methyl derivative of benzene is known as toluene (i.e., “Tolu”, C_7H_8). Depending on where the methyl side-group is attached, a molecule will have several isomers (e.g., monomethyl-pyrene has three isomers in which the $-\text{CH}_3$ group is attached to carbon 1, 2, or 4, respectively). We also indicate whether the structure is a minimum (M) or a transition state (TS) structure for the methyl rotation.

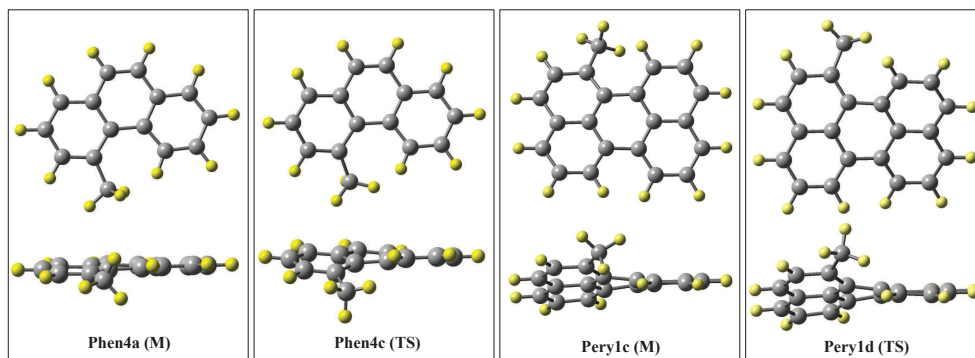


Figure 4: Optimized structures of 4-methylphenanthrene [Phen4a (M) and Phen4c (TS)] and 1-methylperylene [Pery1c (M) and Pery1d (TS)]. H atoms are marked with color yellow and C atoms are color grey. M and TS respectively refer to the minimum (M) or the transition state (TS) structure for the methyl rotation.

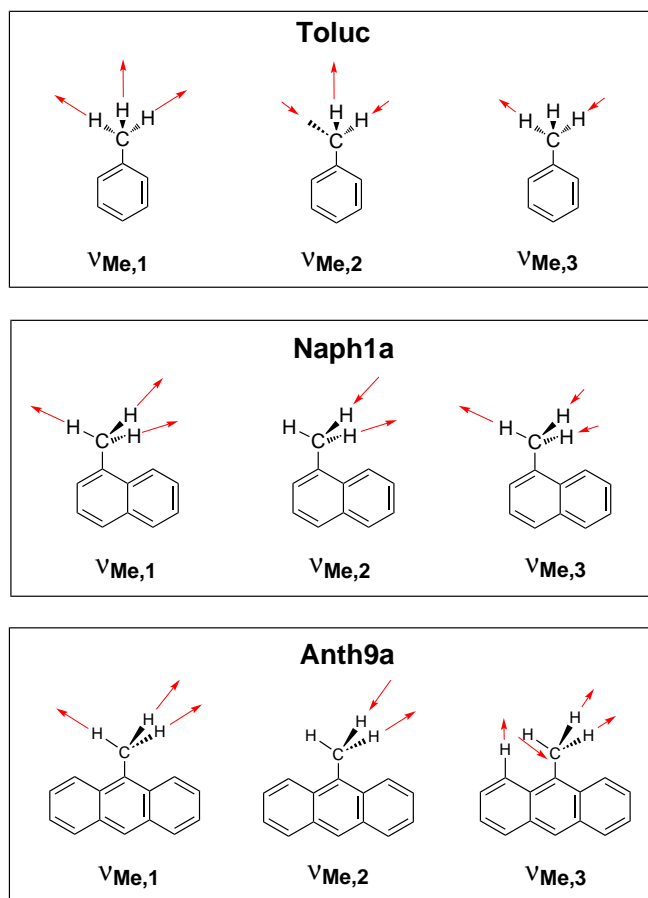


Figure 5: Schematic illustration of the C–H stretching modes of toluene (Toluc, M), naphthalene (Naph1a, M), and anthracene (Anth9a, M). Irrespective of the methyl conformation, $\nu_{\text{Me},1}$ refers to the one symmetric stretching mode in which three CH bonds lengthen/shorten at the same time, $\nu_{\text{Me},2}$ refers to the asymmetric stretching mode in which one CH bond shortens while another lengthens, and $\nu_{\text{Me},3}$ refers to the asymmetric stretching modes in which two CH bonds change in phase and in opposite phase to the third CH bond. These labels are used independently of the frequency of the three modes.

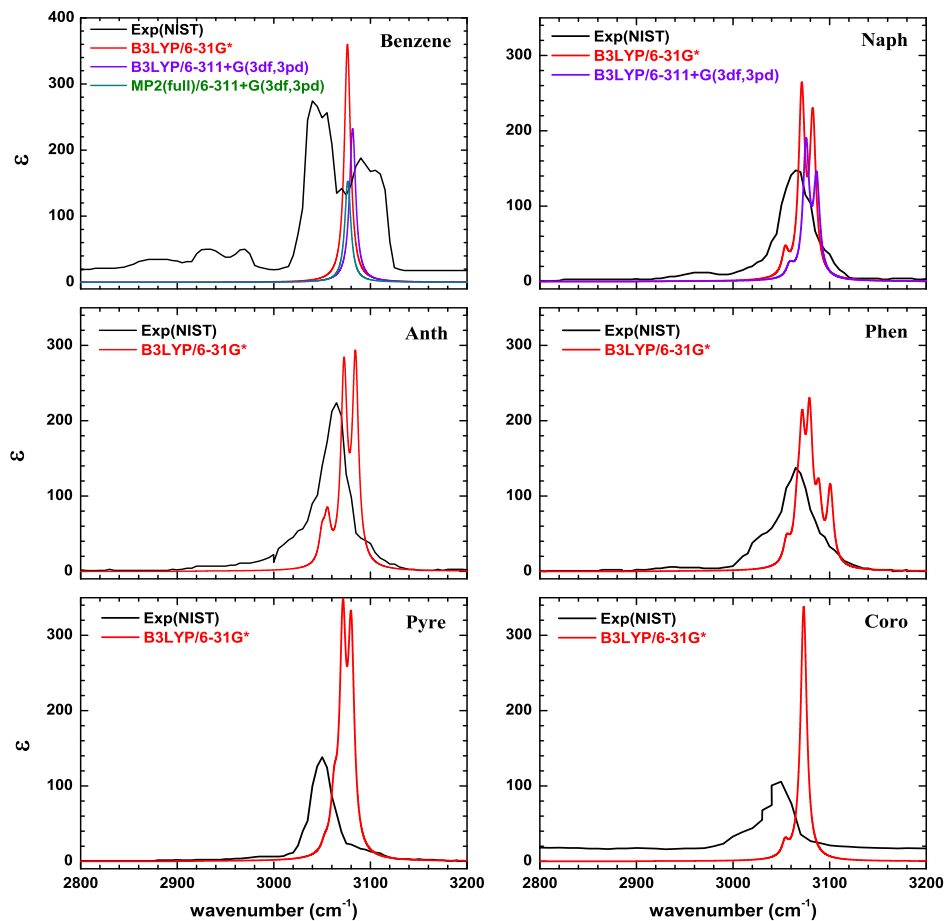


Figure 6: Comparison of the gas-phase absorption spectra experimentally measured by NIST (labelled with “Exp(NIST)”); black lines) to the computed, frequency-scaled spectra (colored lines) of benzene, naphthalene (Naph), anthracene (Anth), phenanthrene (Phen), pyrene (Pyre), and coronene (Coro). The y-axis plots the molar absorptivity coefficient (ϵ) in units of $\text{mol}^{-1} \text{cm}^{-1}$. The ϵ values for the NIST experimental data are scaled to be comparable to the computed values by multiplying the NIST absorbance with an artificial factor, as NIST only gives the absorbance and does not have information for the concentration to derive the absolute ϵ .

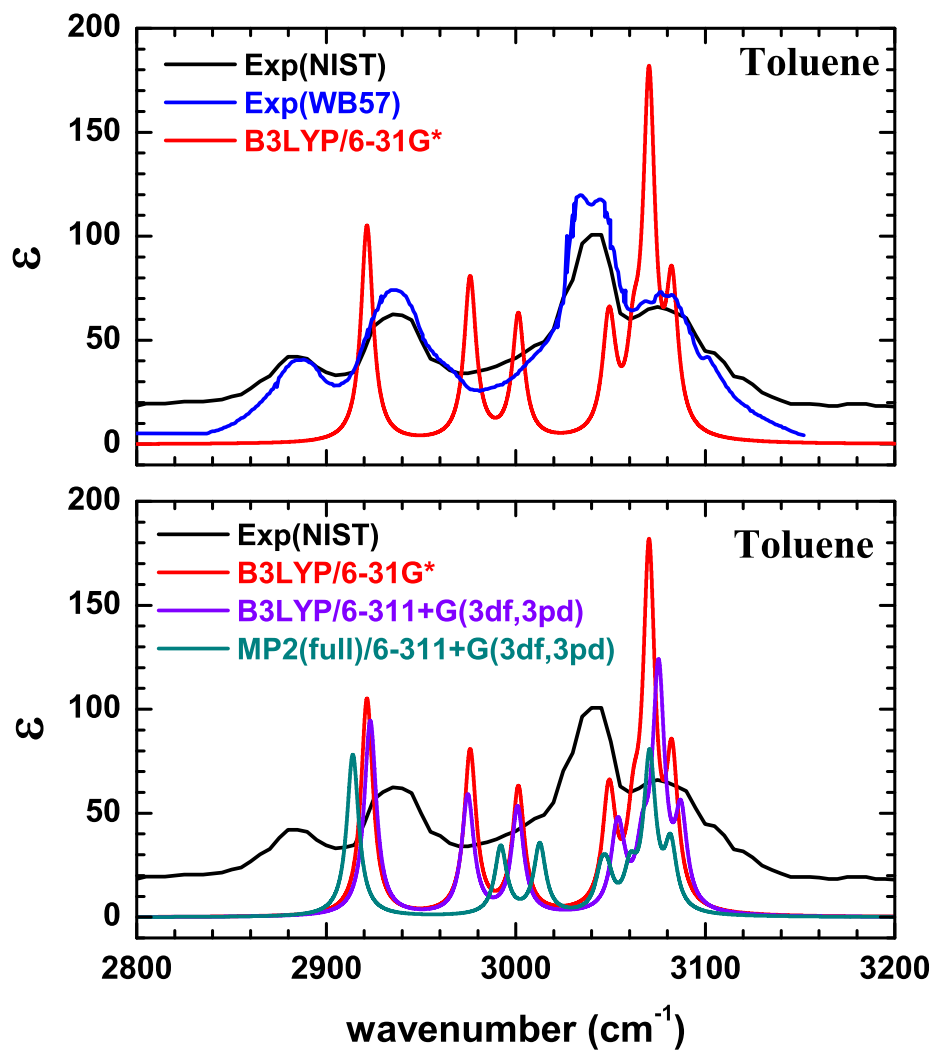


Figure 7: Comparison of the vibrational spectra of toluene computed at various levels with the experimental spectra of NIST [marked with “Exp(NIST)”] and of Wilmshurst & Bernstein (1957) [marked with “Exp(WB57)”]. The NIST and WB57 experimental spectra are multiplied by a factor to be comparable with the computed spectra.

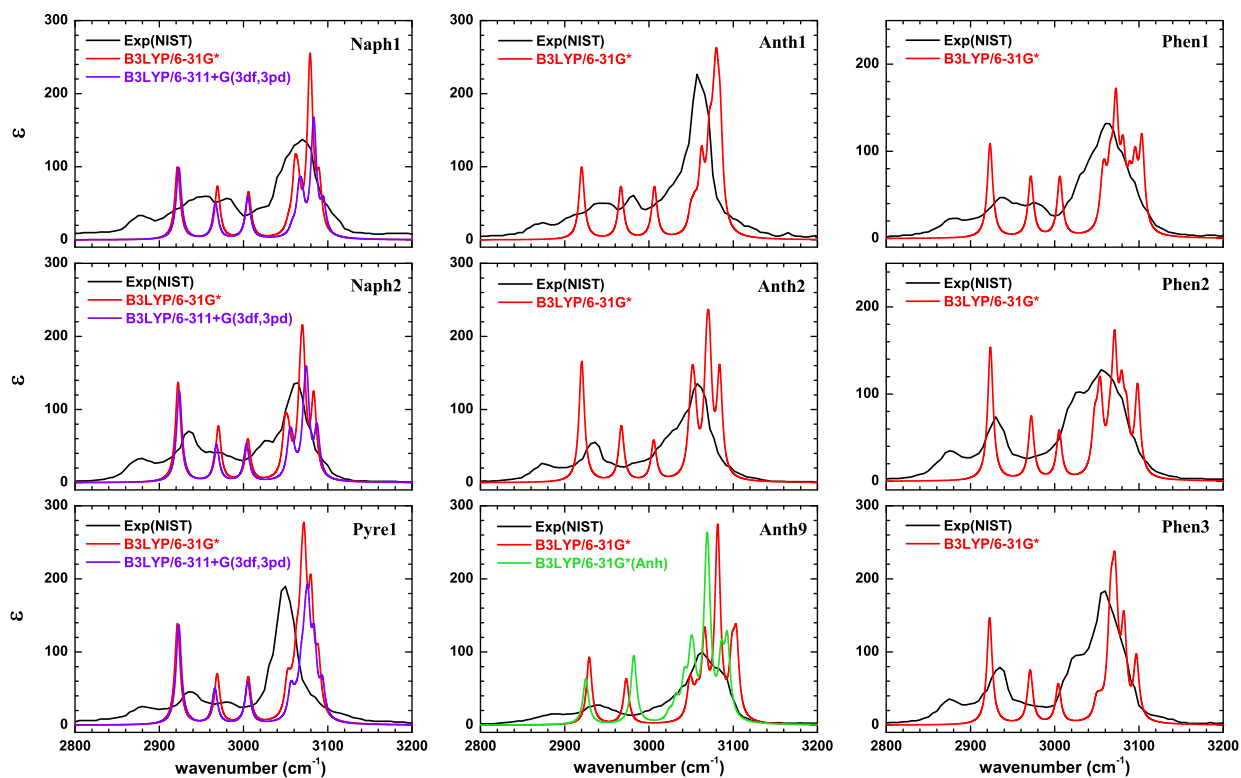


Figure 8: Comparison of the computed spectra of methyl PAHs with their NIST experimental spectra [labelled with “Exp (NIST)”]. The NIST experimental spectra are multiplied by a factor in order to be comparable with the computed spectra.

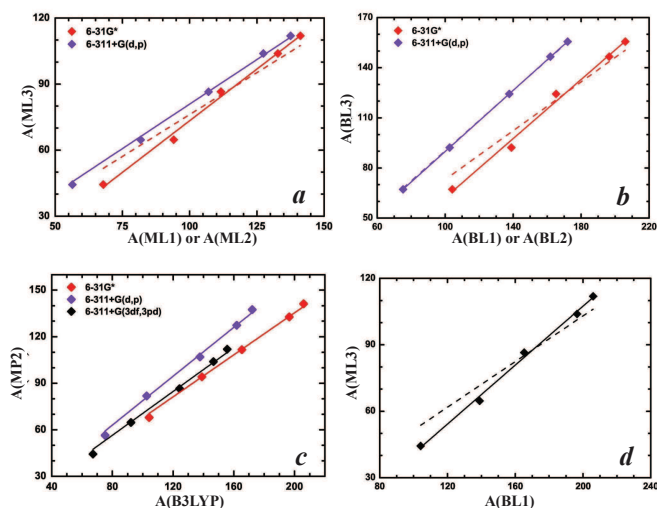


Figure 9: Level dependency of the total C–H stretch intensities (methyl plus aromatic) for benzene and naphthalene and for their methyl derivatives toluene and methylnaphthalene. Top left (a): Intensities calculated at MP2 with small basis sets [i.e., 6-31G* (i.e., *ML1*), 6-311+G(d,p) (i.e., *ML2*)] vs. that with a large basis set [6-311+G(3df,3pd) (i.e., *ML3*)]. Dashed red line plots eq. 1a, solid red line plots eq. 1b, and solid blue line plots eq. 1c. Top right (b): Same as (a) but at B3LYP. Dashed red line plots eq. 2a, solid red line plots eq. 2b, dashed blue line plots eq. 2c, and solid blue line plots eq. 2d. Bottom left (c): Intensities calculated at B3LYP vs. MP2 with the same basis set. Solid red line plots eq. 3a, solid blue line plots eq. 3b, and solid black line plots eq. 3c. Bottom right (d): Intensities calculated at B3LYP/6-31G* (i.e., *BL1*) vs. MP2/6-311+G(3df,3pd) (i.e., *ML3*). Dashed black line plots eq. 4a, and solid black line plots eq. 4b

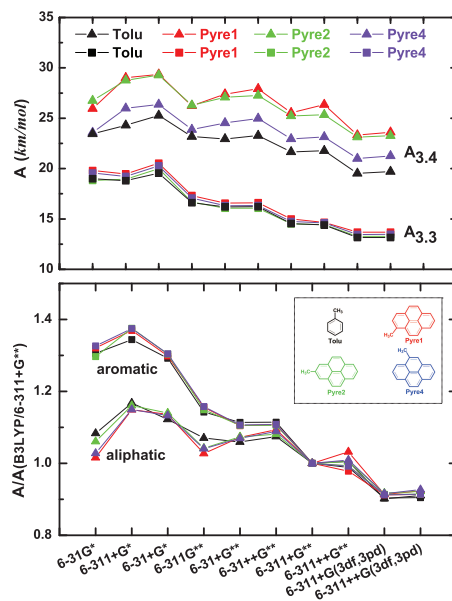


Figure 10: Top: Absolute intensities of the methyl (aliphatic) C–H stretch per chemical bond ($A_{3.4}$; triangles) and of the aromatic C–H stretch ($A_{3.3}$; squares) for toluene and the three isomers of methyl pyrene computed at the B3LYP level with different basis sets. Bottom: Relative intensities of $A_{3.4}$ and $A_{3.3}$ computed at different basis sets with respect to those at B3LYP/6-311+G** (i.e., our standard level).

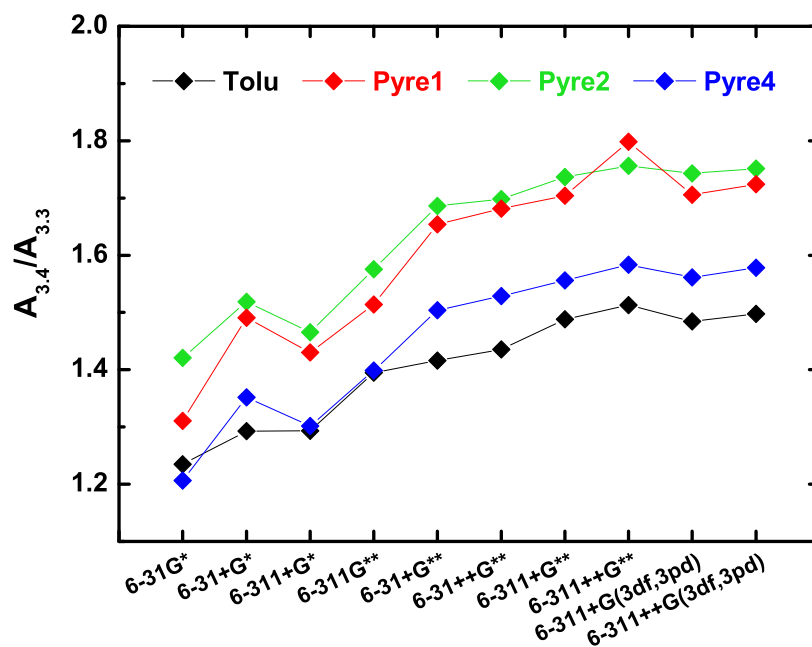


Figure 11: Band-strength ratios ($A_{3.4}/A_{3.3}$) computed with different basis sets for toluene (i.e., methylbenzene) and the three isomers of methylpyrene. From left to right, the computations become increasingly more computer-time intensive and the results are expected to be more accurate. The results computed with the B3LYP method and in conjunction with the basis sets 6-311+G**, 6-311++G**, 6-311+G(3df,3pd), and 6-311++G(3df,3pd) have essentially reached the convergence limit. For a compromise between accuracy and computational demand, the method of B3LYP/6-311+G** is preferred.

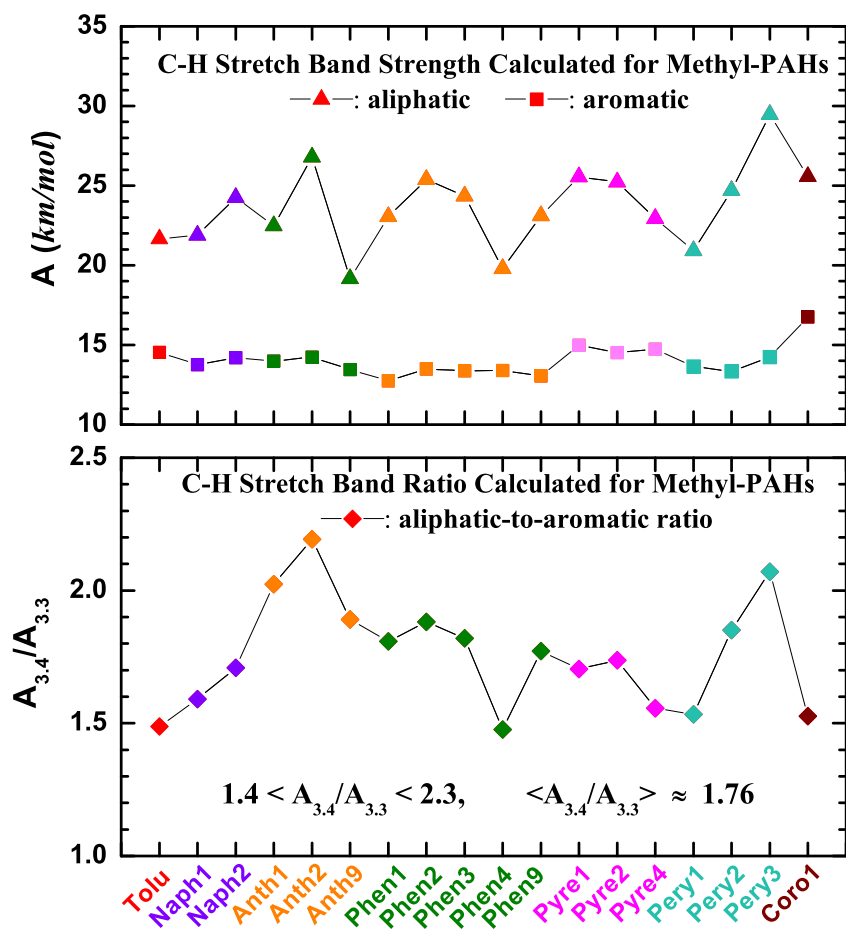


Figure 12: Band-strength as determined with the B3LYP/6-311+G** method for the mono-methyl derivatives of seven aromatic molecules and all of their isomers (benzene, naphthalene, anthracene, phenanthrene, pyrene, perylene, and coronene).

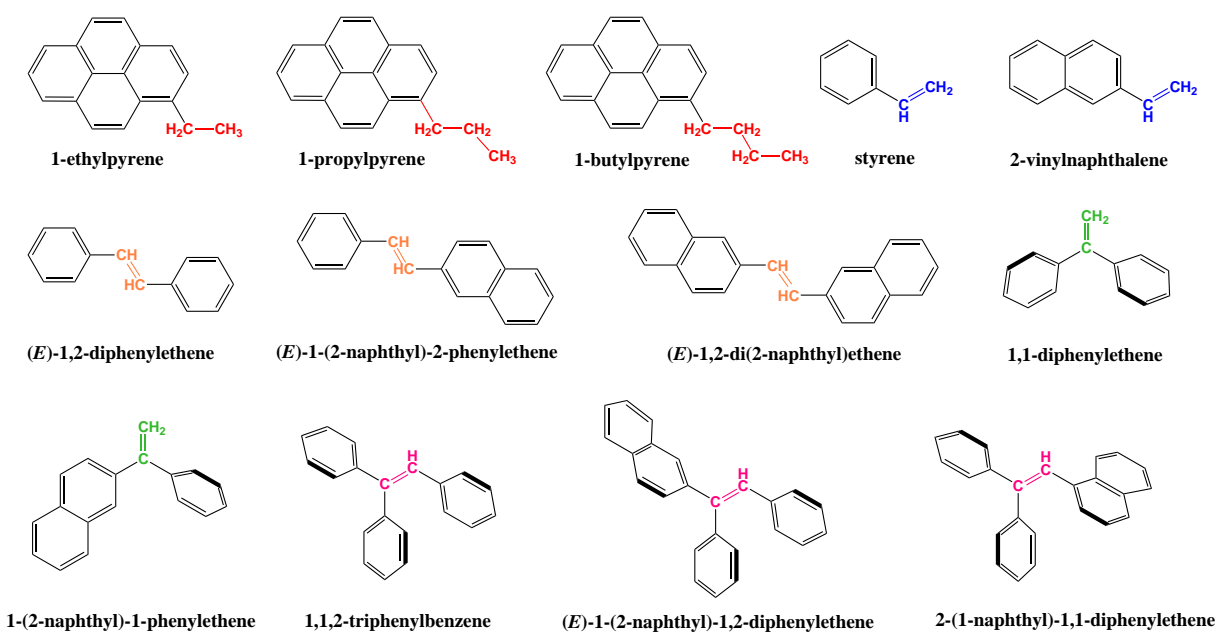


Figure 13: Structures of PAHs attached with sidegroups other than methyl: ethyl ($-\text{CH}_2-\text{CH}_3$), propyl ($-\text{CH}_2-\text{CH}_2-\text{CH}_3$), butyl ($-\text{CH}_2-\text{CH}_2-\text{CH}_2-\text{CH}_3$), and unsaturated alkyl chains ($-\text{CH}=\text{CH}_2$, $-\text{CH}=\text{CH}-$, $\text{C}=\text{CH}_2$, $\text{C}=\text{C}-\text{H}$).

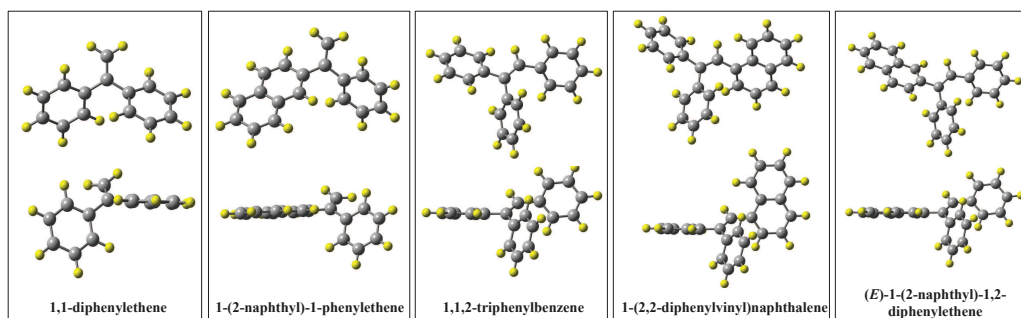


Figure 14: Optimized structures of phenyl- and naphthyl-substituted ethene. H atoms are shown in yellow and C atoms in grey. All structures are minima.

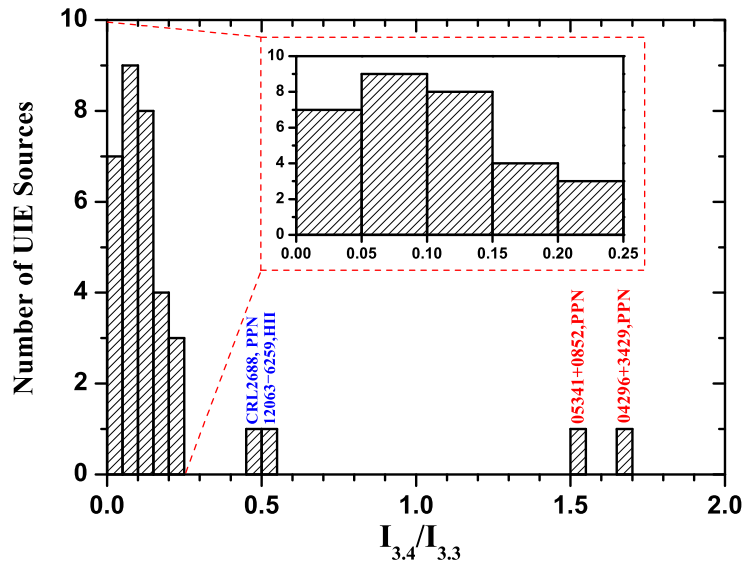


Figure 15: Histogram of the flux ratio ($I_{3.4}/I_{3.3}$) for 35 UIE sources. The median flux ratio is $\langle I_{3.4}/I_{3.3} \rangle \approx 0.12$. The insert panel enlarges the flux ratio distribution for the 31 sources with $I_{3.4}/I_{3.3} \lesssim 0.25$.

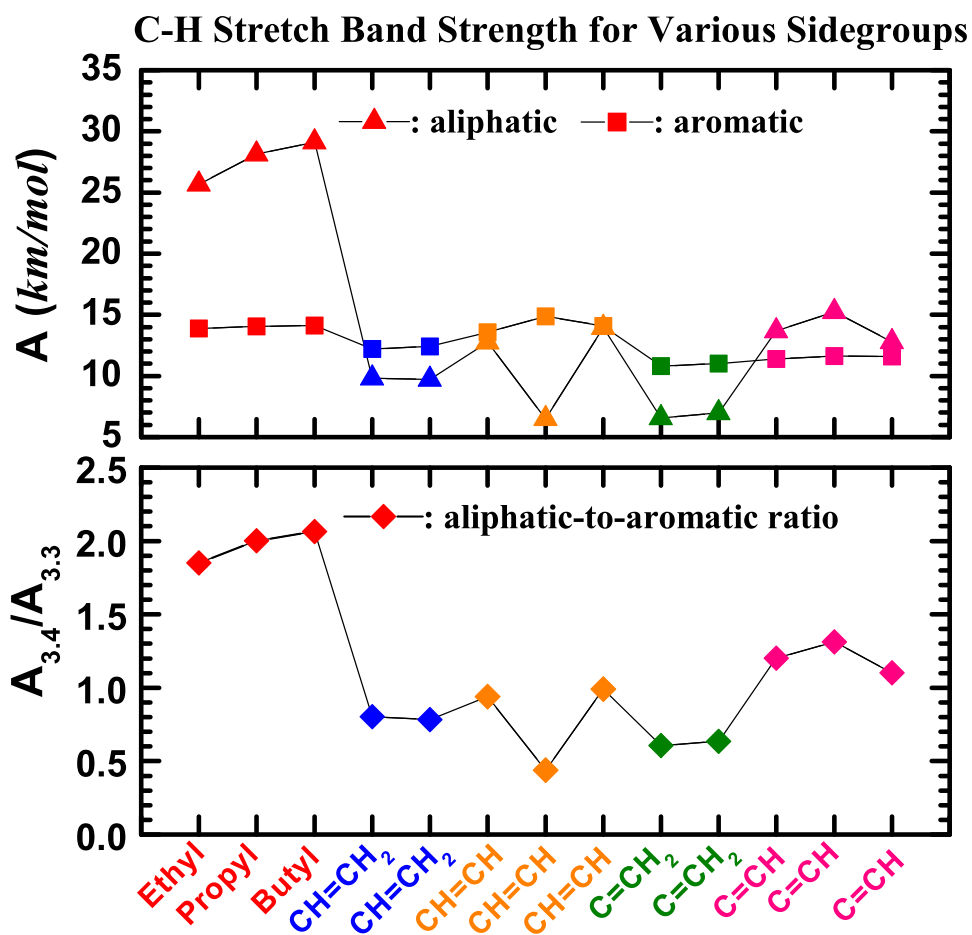


Figure 16: Band-strengths as determined with the B3LYP/6-311+G** method for PAHs with sidegroups other than methyl: ethyl (-CH₂-CH₃), propyl (-CH₂-CH₂-CH₃), butyl (-CH₂-CH₂-CH₂-CH₃), and unsaturated alkyl chains (-CH=CH₂, -CH=CH-, C=CH₂, C=C-H).

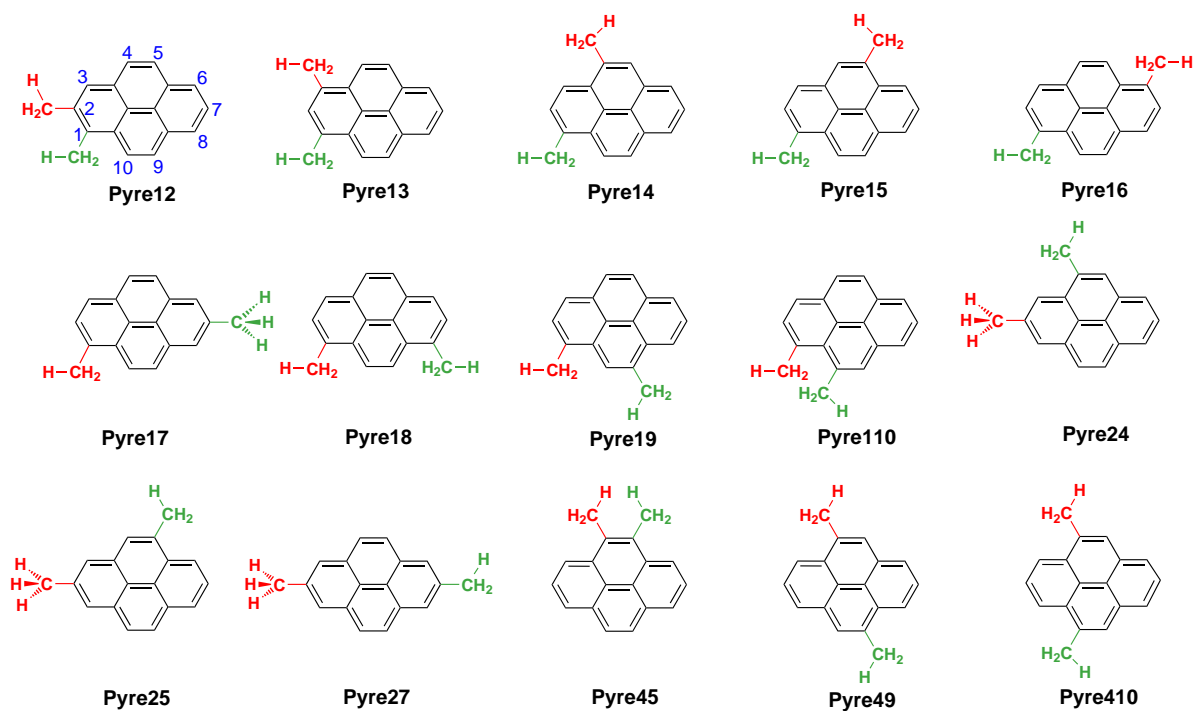


Figure 17: Structures of all isomers of dimethylpyrene. The same naming method is used as in Figure 3: “Pyre” stands for pyrene, and the digits specify the locations of the attached methyl groups (e.g., “Pyre110” means the two methyl groups are attached at positions 1 and 10).

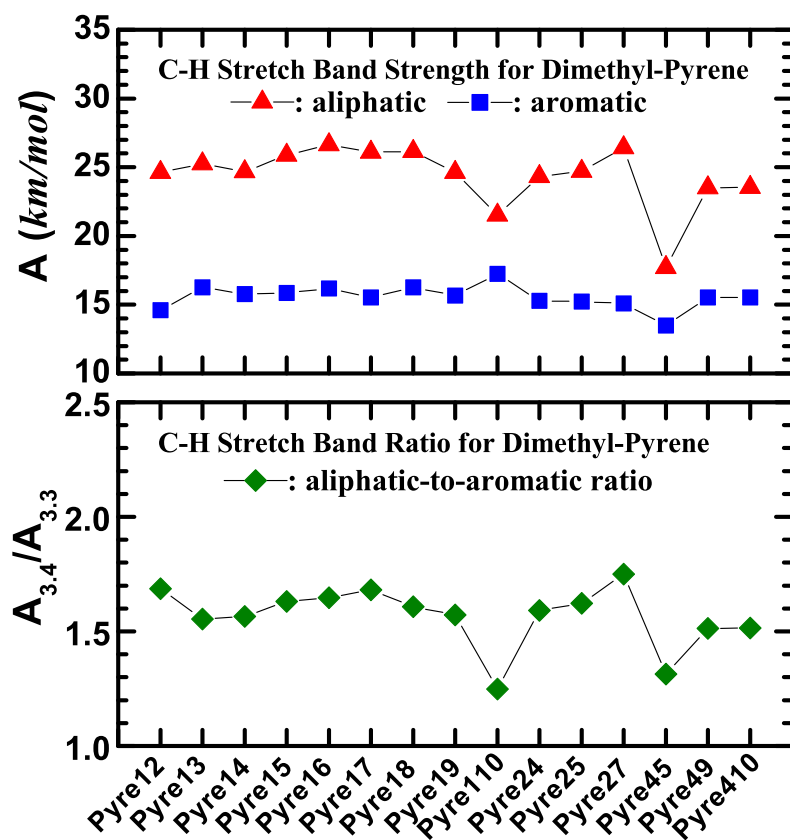


Figure 18: Band-strength as determined with the B3LYP/6-311+G** method for all the isomers of dimethyl pyrene.

Table 1: Standard scale factors for computed vibrational frequencies.

Basis set	B3LYP	MP2
6-31G*	0.9613 ^a	
6-31+G*	0.9640 ^b	
6-311+G*	0.9678 ^c	
6-311G**	0.9670 ^b	
6-31+G**	0.9640 ^b	
6-31++G**	0.9640 ^b	
6-311+G**	0.9688 ^a	0.9523 ^a
6-311++G**	0.9679 ^c	
6-311+G(3df,3pd)	0.9672 ^d	0.9540 ^a
6-311++G(3df,3pd)	0.9673 ^d	

^a Borowski (2012)

^b Precomputed vibrational scaling factors taken from the *Computational Chemistry Comparison and Benchmark Database* (CCVCBC). Online at <http://cccbdb.nist.gov/vibscalejust.asp> (accessed 06/01/13)

^c Andersson et al. 2005

^d Merrick et al. 2007

Table 2: Computed total energies and thermochemical parameters for the minima of all the methyl PAHs shown in Figure 3 at B3LYP/6-31G*.

Compound	$E_{\text{tot}}^{\text{a}}$	VZPE ^b	TE ^c	S^{d}	ν_1^{e}	ν_2^{e}	μ^{f}
Toluc	-271.566650	80.53	84.42	79.27	42.95	211.45	0.3196
Naph1a	-425.209691	110.36	115.62	89.08	135.46	170.33	0.2956
Naph2b	-425.211193	110.11	115.49	90.50	95.66	125.11	0.4170
Anth1a	-578.847859	139.67	146.59	102.01	91.96	93.37	0.2897
Anth2b	-578.849214	139.39	146.43	103.32	71.42	111.02	0.4971
Anth9a	-578.842107	139.61	146.67	104.52	37.81	106.76	0.3224
Phen1a	-578.854850	139.86	146.78	102.32	69.98	98.69	0.2931
Phen2b	-578.857120	139.56	146.64	104.24	69.47	80.52	0.4800
Phen3b	-578.856977	139.59	146.66	104.21	71.92	79.29	0.4748
Phen4a	-578.845615	140.23	147.03	102.47	34.77	91.70	0.2896
Phen9a	-578.855626	139.94	146.84	102.02	85.30	99.09	0.3250
Pyre1a	-655.089741	147.89	155.21	104.58	86.96	117.44	0.4176
Pyre2c	-655.091084	147.55	155.06	107.98	32.65	76.60	0.4572
Pyre4a	-655.090587	147.93	155.22	104.23	88.52	126.68	0.3563
Pery1c	-808.713736	177.50	186.40	116.34	60.05	81.63	0.4009
Pery2a	-808.724609	176.97	186.23	121.10	25.21	82.46	0.4250
Pery3a	-808.722947	177.13	186.31	122.62	6.21	72.41	0.4337
Coro1a	-961.214987	193.45	203.31	122.27	71.73	89.44	0.4294

^a Total energies in atomic units.

^b Vibrational zero-point energies (VZPE) in kcal mol^{-1} .

^c Thermal energies (TE) in kcal mol^{-1} .

^d Molecular entropies (S) in $\text{cal mol}^{-1} \text{K}^{-1}$.

^e The lowest vibrational modes ν_1 and ν_2 in cm^{-1} .

^f Dipole moment in Debye.

Table 3: Computed total energies and thermochemical parameters for the transition states of the methyl PAHs shown in Figure 3 at B3LYP/6-31G*. Note that the transition state has an imaginary frequency (i.e., ν_1) which is sometimes negative.

Compound	E_{tot}	VZPE	TE	S	ν_1	ν_2	μ
Tolua	-271.566621	80.46	83.82	74.15	-33.24	212.77	0.3218
Naph1b	-425.206459	110.10	115.00	86.92	-184.14	122.52	0.3865
Naph2a	-425.210243	109.96	114.88	87.05	-105.36	118.80	0.4218
Anth1b	-578.844198	139.39	145.96	99.97	-205.78	85.65	0.4125
Anth2a	-578.847870	139.24	145.83	100.10	-117.02	72.64	0.5099
Anth9c	-578.842064	139.60	146.13	99.50	-56.97	84.56	0.3059
Phen1b	-578.851600	139.56	146.15	100.48	-188.17	61.85	0.4120
Phen2a	-578.856498	139.44	146.03	100.28	-87.20	74.80	0.4752
Phen3a	-578.856363	139.47	146.05	100.23	-80.21	77.31	0.4686
Phen4c	-578.838725	139.68	146.20	99.60	-205.94	79.23	0.2660
Phen9b	-578.851402	139.60	146.18	100.34	-212.72	80.36	0.4080
Pyre1b	-655.087304	147.66	154.60	102.20	-157.10	83.70	0.5462
Pyre2a	-655.091051	147.49	154.45	102.31	-16.07	77.15	0.4598
Pyre4b	-655.086624	147.68	154.62	102.24	-208.36	81.97	0.4647
Pery1d	-808.707553	177.09	185.72	114.66	-220.94	66.36	0.4084
Pery2b	-808.723876	176.86	185.63	117.28	-89.40	25.41	0.4541
Pery3b	-808.719443	176.89	185.69	118.48	-193.39	17.37	0.6114
Coro1b	-961.211602	193.22	202.72	120.08	-194.54	68.28	0.5411

Table 4: Same as Table 2 but at the B3LYP/6-311+G** level.

Compound	E_{tot}	VZPE	TE	S	ν_1	ν_2	μ
Benzene	-232.311242	62.84	65.61	64.13	409.45	409.45	0.0000
Toluc	-271.638814	79.90	83.80	79.24	44.80	208.95	0.4056
Naph	-385.988871	92.17	96.46	79.31	173.26	185.09	0.0000
Naph1a	-425.315358	109.49	114.79	89.37	131.97	164.79	0.3704
Naph2b	-425.316894	109.27	114.67	90.66	93.95	123.71	0.5180
Anth	-539.660248	121.27	127.22	95.16	91.25	120.32	0.0000
Anth1a	-578.987081	138.58	145.54	102.39	90.23	90.87	0.3688
Anth2b	-578.988540	138.33	145.40	103.61	69.69	108.40	0.6126
Anth9a	-578.981699	138.56	145.67	105.09	35.51	99.39	0.3669
Phen	-539.668406	121.51	127.46	94.01	95.52	99.88	0.0154
Phen1a	-578.994150	138.82	145.80	102.68	68.76	97.16	0.3927
Phen2b	-578.996368	138.53	145.65	104.51	68.39	79.96	0.5846
Phen3b	-578.996254	138.57	145.67	104.39	72.49	79.37	0.5647
Phen4a	-578.984766	139.13	145.98	102.64	38.29	90.02	0.3458
Phen9a	-578.994871	138.88	145.84	102.41	83.88	96.66	0.4309
Pyre	-615.915984	129.36	135.70	94.90	97.80	151.01	0.0000
Pyre1a	-655.242211	146.67	154.06	105.09	84.94	115.06	0.5126
Pyre2c	-655.243498	146.32	153.89	108.34	34.24	74.34	0.5614
Pyre4a	-655.243011	146.69	154.06	104.76	86.08	123.96	0.4367
Pery	-769.582201	158.55	166.73	111.71	24.99	94.75	0.0000
Pery1c	-808.899758	176.07	185.06	116.99	59.11	80.06	0.5012
Pery2a	-808.910315	175.56	184.89	121.35	27.21	85.03	0.5198
Pery3a	-808.908572	175.70	184.96	121.79	13.26	70.40	0.5330
Coro	-922.100621	174.27	183.26	116.26	86.41	86.81	0.0007
Coro1a	-961.427339	191.61	201.64	123.33	70.24	87.85	0.5207

Table 5: Calculated frequencies and intensities for methyl (aliphatic) C–H and aromatic C–H stretches of toluene at the most pertinent levels and comparison to the NIST gas-phase experimental values.

		B3LYP/6-31G*			NIST		WD57 ^g			
	$\nu(\text{cal})^{\text{a}}$	ν^{b}	$A(\text{cal})^{\text{c}}$	$\nu(\text{exp})^{\text{d}}$	$A_{\text{ali}}/A_{\text{aro}}^{\text{e}}$	$A(\text{exp})^{\text{f}}$	$\nu(\text{exp})^{\text{d}}$	$A_{\text{ali}}/A_{\text{aro}}^{\text{e}}$	$A(\text{exp})^{\text{f}}$	
$\nu_{\text{Me},1}^{\text{h}}$	3039.1	2921.5	30.3	(2884.2)	0.79	42.9	(2885.8)	0.71	–	
$\nu_{\text{Me},2}^{\text{h}}$	3095.8	2975.9	22.7	(2935.4)			(2936.2)			
$\nu_{\text{Me},3}^{\text{h}}$	3122.2	3001.4	17.4							
	3171.3	3048.6	10.2							
	3173.1	3050.3	6.9							
$\nu_{\text{aro}}^{\text{i}}$	3185.4	3062.2	9.8	(3040.7)		54.3	(3039.4)		–	
	3194.0	3070.3	48.4	(3076.9)			(3079.6)			
	3206.6	3082.5	19.7							
		B3LYP/6-311+G**			B3LYP/6-311+G(3df,3pd)			MP2(full)/6-311+G**		
	$\nu(\text{cal})^{\text{a}}$	ν^{b}	$A(\text{cal})^{\text{c}}$	$\nu(\text{cal})^{\text{a}}$	ν^{b}	$A(\text{cal})^{\text{c}}$	$\nu(\text{cal})^{\text{a}}$	ν^{b}	$A(\text{cal})^{\text{c}}$	
$\nu_{\text{Me},1}^{\text{h}}$	3019.8	2925.5	28.9	3022.4	2923.2	27.2	3072.7	2926.1	25.8	
$\nu_{\text{Me},2}^{\text{h}}$	3073.5	2977.7	19.4	3075.6	2974.7	16.6	3151.3	3001.0	13.2	
$\nu_{\text{Me},3}^{\text{h}}$	3099.3	3002.6	16.7	3102.7	3001.0	14.8	3170.3	3019.1	12.1	
	3151.8	3053.5	9.0	3156.6	3053.0	7.6	3195.3	3042.9	7.2	
	3153.4	3055.0	6.0	3158.7	3055.1	5.2	3197.1	3044.6	6.2	
$\nu_{\text{aro}}^{\text{i}}$	3166.1	3067.3	7.2	3171.0	3067.0	7.4	3211	3057.8	4.0	
	3174.4	3075.3	36.4	3179.7	3075.4	32.9	3219.8	3066.2	26.8	
	3186.9	3087.5	14.2	3191.9	3087.2	12.6	3232.3	3078.1	11.9	

^a Computed frequency in cm^{-1} .

^b Frequency scaled with the corresponding scaling factors listed in Table 1.

^c Computed intensity in km mol^{-1} .

^d Experimental frequency in cm^{-1} (they are given in parentheses as they may not necessarily correspond to $\nu_{\text{Me},x}$ or ν_{aro}).

^e Ratio of the total methyl (aliphatic) C–H stretch intensity to the combined intensity of all aromatic C–H stretches as described in §4.2.

^f Experimental intensity in km mol^{-1} .

^g Wilmschurst & Bernstein (1957).

^h Methyl (aliphatic) C–H stretch frequencies as described in the beginning of §4.

ⁱ Aromatic C–H stretch frequencies.

Table 6: IR intensities (km mol^{-1}) computed with the B3LYP and MP2 methods with different basis sets for benzene, toluene, and 1- and 2-methyl naphthalene [ML0: MP2/6-311G(3df,3pd); BL1: B3LYP/6-31G*, BL2: B3LYP/6-311+G**, BL3: B3LYP/6-311+G(3df,3pd); ML1: MP2/6-31G*, ML2: MP2/6-311+G**, ML3: MP2/6-311+G(3df,3pd)].

		Exp ^a	ML0 ^b	ML0(fc)	ML0(full)	BL1	BL2	BL3	ML1	ML2	ML3
Benzene	A	55	53	53.83	52.38	104.00	75.16	67.23	67.88	56.40	44.27
	A ^c	95	98	97.08	94.73	165.30	137.70	124.32	111.55	107.04	86.53
Tolu	A _{3,4} ^d			44.25	43.19	70.40	64.96	58.57	47.17	51.04	41.83
	A _{3,3} ^e			52.83	51.53	94.90	72.74	65.75	64.38	56.00	44.69
	A _{3,4} /A _{3,3}					1.24	1.49	1.48	1.22	1.52	1.56
	A ^c					196.50	161.92	146.64	132.77	127.39	103.87
Naph1	A _{3,4} ^d					67.70	65.66	59.48	43.44	49.90	41.94
	A _{3,3} ^e					128.80	96.27	87.16	89.33	77.49	61.93
	A _{3,4} /A _{3,3}					1.23	1.59	1.59	1.13	1.50	1.58
	A ^c					206.00	172.08	155.60	141.23	137.45	111.88
Naph2	A _{3,4} ^d					77.60	72.75	65.58	44.34	55.29	46.45
	A _{3,3} ^e					128.40	99.32	90.02	96.89	82.16	65.43
	A _{3,4} /A _{3,3}					1.41	1.71	1.70	1.07	1.57	1.66
	A ^c										

^a Experimental values listed in Pavlyuchko et al. (2012).

^b Computed values of Pavlyuchko et al. (2012) at the MP2/6-311G(3df,3pd) (i.e., ML0) level.

^c $A = A_{3,4} + A_{3,3}$.

^d Intensity of the methyl (aliphatic) C–H stretch (per chemical bond).

^e Intensity of the aromatic C–H stretch (per chemical bond).

Table 7: Averages of scaled, characteristic frequencies and intensities of the aliphatic and aromatic C–H stretches for toluene and all the isomers of methyl pyrene computed at B3LYP with different basis sets.

	Basis Set	$\bar{\nu}_{3.4}^a$	$\sigma(\nu_{3.4})^b$	$\bar{\nu}_{3.3}^a$	$\sigma(\nu_{3.3})^b$	$A_{3.4}^c$	$\sigma(A_{3.4})^d$	$A_{3.3}^c$	$\sigma(A_{3.3})^d$	$A_{3.4}/A_{3.3}$
Tolu	6-31G*	2966.3	40.8	3062.8	14.2	23.5	6.5	19.0	17.1	1.23
	6-31+G*	2968.9	39.2	3068.7	14.4	24.3	8.0	18.8	16.4	1.29
	6-31+G**	2968.3	41.7	3068.2	14.2	22.9	8.2	16.2	13.9	1.42
	6-31++G**	2968.0	41.9	3068.0	14.2	23.3	8.4	16.2	14.1	1.44
	6-311G**	2965.5	39.6	3063.2	14.3	23.2	5.6	16.6	14.7	1.39
	6-311+G*	2967.7	38.0	3062.7	14.5	25.3	6.8	19.6	17.5	1.29
	6-311+G**	2968.6	39.3	3067.7	14.3	21.7	6.4	14.5	12.6	1.49
	6-311++G**	2965.7	39.4	3064.6	14.2	21.8	6.6	14.4	12.5	1.51
	6-311+G(3df,3pd)	2966.3	39.5	3067.5	14.3	19.5	6.7	13.1	11.4	1.48
6-311++G(3df,3pd)	2966.5	39.6	3068.0	14.2	19.7	6.6	13.2	11.4	1.50	
Pyre1	6-31G*	2965.3	42.1	3065.7	12.8	25.9	12.1	19.8	17.6	1.31
	6-31+G*	2966.2	40.4	3071.6	13.1	29.0	16.8	19.5	16.6	1.49
	6-31+G**	2965.3	43.1	3071.4	12.9	27.4	16.7	16.6	13.9	1.65
	6-31++G**	2966.5	43.3	3070.9	12.8	27.9	16.3	16.6	14.1	1.68
	6-311G**	2964.4	41.3	3066.4	12.7	26.2	12.1	17.3	15.0	1.51
	6-311+G*	2966.6	39.2	3066.0	13.0	29.4	15.0	20.5	18.1	1.43
	6-311+G**	2967.3	40.9	3070.5	12.6	25.5	14.0	15.0	12.7	1.70
	6-311++G**	2964.4	40.9	3067.4	12.6	26.4	14.7	14.7	12.4	1.80
	6-311+G(3df,3pd)	2964.7	40.9	3070.2	12.8	23.3	14.0	13.7	11.5	1.71
6-311++G(3df,3pd)	2964.9	41.1	3070.6	12.8	23.6	14.1	13.7	11.5	1.72	
Pyre2	6-31G*	2969.2	41.2	3060.7	11.2	26.8	14.7	18.8	26.2	1.42
	6-31+G*	2970.1	39.3	3066.1	11.6	28.8	17.4	18.9	25.4	1.52
	6-31+G**	2969.5	41.9	3066.0	11.4	27.1	17.2	16.1	21.8	1.69
	6-31++G**	2970.6	42.2	3065.8	11.2	27.3	17.3	16.1	22.0	1.70
	6-311G**	2968.1	40.0	3061.6	11.0	26.3	13.2	16.7	23.6	1.58
	6-311+G*	2970.1	38.4	3061.0	11.2	29.3	15.7	20.0	27.6	1.47
	6-311+G**	2970.9	39.7	3065.7	11.0	25.2	14.2	14.5	20.4	1.74
	6-311++G**	2968.1	39.7	3062.6	11.0	25.3	14.4	14.4	20.3	1.76
	6-311+G(3df,3pd)	2968.3	39.8	3065.4	10.8	23.1	13.9	13.3	18.5	1.74
6-311++G(3df,3pd)	2968.5	39.9	3065.9	10.8	23.3	13.9	13.3	18.6	1.75	
Pyre4	6-31G*	2963.8	43.2	3066.6	14.5	23.6	9.8	19.6	18.1	1.21
	6-31+G*	2966.1	41.4	3072.2	14.8	26.0	13.6	19.2	17.0	1.35
	6-31+G**	2965.2	44.0	3072.0	14.6	24.5	13.4	16.3	14.5	1.50
	6-31++G**	2965.0	44.1	3071.9	14.6	25.0	13.4	16.3	14.7	1.53
	6-311G**	2962.8	42.2	3067.6	14.4	23.9	9.8	17.1	16.3	1.40
	6-311+G*	2965.1	40.0	3067.0	14.7	26.4	12.2	20.3	19.1	1.30
	6-311+G**	2965.8	41.7	3071.7	14.4	22.9	11.4	14.7	13.8	1.56
	6-311++G**	2962.8	41.6	3068.6	14.4	23.2	11.7	14.6	13.8	1.58
	6-311+G(3df,3pd)	2963.1	41.7	3071.5	14.6	21.0	11.5	13.5	12.5	1.56
6-311++G(3df,3pd)	2963.3	41.8	3072.0	14.6	21.3	11.5	13.5	12.5	1.58	

^a Average scaled frequency for the methyl (aliphatic) or aromatic C–H stretch in cm^{-1}

^b Standard deviation of frequency for the methyl or aromatic C–H stretch in cm^{-1}

^c Intensity of each C–H bond for the methyl or aromatic C–H stretch in km mol^{-1}

^d Standard deviation of intensity of each C–H bond for the methyl or aromatic C–H stretches in km mol^{-1}

Table 8: Averages of scaled, characteristic frequencies and intensities of the aliphatic and aromatic C–H stretches of PAHs and their methyl derivatives computed at B3LYP/6-311+G** (with the same units as that in Table 7)

	$\bar{\nu}_{3.4}$	$\sigma(\nu_{3.4})$	$\bar{\nu}_{3.3}$	$\sigma(\nu_{3.3})$	$A_{3.4}$	$\sigma(A_{3.4})$	$A_{3.3}$	$\sigma(A_{3.3})$	$A_{3.4}/A_{3.3}$	$(A_{3.4}/A_{3.3})_{\text{NIST}}$
Benzene			3077.3	12.8			12.5	19.4		
Toluc	2968.6	39.3	3067.7	14.3	21.7	6.4	14.5	12.6	1.49	1.32
Naph			3071.0	12.2			12.8	22.3		
Naph1a	2967.6	40.9	3073.7	13.8	21.9	7.1	13.8	10.0	1.59	1.66
Naph2b	2967.8	39.9	3066.5	12.6	24.3	12.4	14.2	11.6	1.71	1.89
Anth			3070.0	12.4			13.2	22.9		
Anth1a	2966.5	41.9	3071.0	12.1	22.5	6.8	14.0	11.1	2.02	1.77
Anth2b	2966.1	41.2	3064.8	11.9	26.8	17.1	14.2	12.2	2.19	1.62
Anth9a	2985.0	59.4	3078.8	18.6	19.2	8.6	13.5	10.1	1.89	1.26
Phen			3077.0	15.9			12.4	14.6		
Phen1a	2969.2	40.4	3080.5	17.7	23.1	8.5	12.7	8.3	1.81	1.50
Phen2b	2969.0	39.4	3072.8	17.4	25.4	15.3	13.5	9.0	1.88	1.62
Phen3b	2967.8	39.2	3073.4	15.2	24.3	14.3	13.4	11.9	1.82	1.53
Phen4a	2973.7	39.2	3084.9	40.8	19.8	3.4	13.4	13.4	1.48	
Phen9a	2967.9	41.5	3079.8	17.7	23.1	10.8	13.0	7.7	1.77	
Pyre			3069.6	10.4			14.0	25.3		
Pyre1a	2967.3	40.9	3070.5	12.6	25.5	14.0	15.0	12.7	1.70	1.59
Pyre2c	2970.9	39.7	3065.7	11.0	25.2	14.2	14.5	20.4	1.74	
Pyre4a	2965.8	41.7	3071.7	14.4	22.9	11.4	14.7	13.8	1.56	
Pery			3084.1	17.3			13.2	26.8		
Pery1c	2970.3	45.6	3083.0	25.1	20.9	9.9	13.6	15.1	1.53	
Pery2a	2968.8	39.5	3079.8	17.2	24.7	14.4	13.3	13.9	1.85	
Pery3a	2966.4	41.4	3084.1	17.7	29.5	20.5	14.2	13.5	2.07	
Coro			3068.7	9.1			16.2	35.2		
Coro1a	2968.1	41.4	3068.9	11.8	25.6	15.5	16.8	21.8	1.53	

